Numerical modelling of ink penetration and moisture-induced deformations in coated paper sheets

Leemans, Lars H.W.

Award date:
2024

Eindhoven University of Technology

Department of Mechanical Engineering

Numerical modelling of ink penetration and moisture-induced deformations in coated paper sheets

Master Thesis

By:
L.H.W. Leemans

ID Number:
1238509

Committee:

Thesis Supervisor:	dr.ir. R.H.J. Peerlings
Second Supervisor:	C.A. Rojas Vega, MSc.
Chairman:	dr.ir. O. Rokos
Member external group:	prof.dr. J.G.M. Kuerten
Advisor:	dr.ir. T. Anijs

This report was made in accordance with the TU/e Code of Scientific Conduct for the Master thesis

Eindhoven May 10, 2024

Abstract

In modern day digital printing systems, water based inks are favored for their cost-effectiveness, environmental friendliness and versatility. However, their high water content can cause them to infiltrate paper sheets and invade the cellulose fibers. This invasion causes the fibers to swell which can in turn lead to dimensional instabilities in the printing process. The application of a coating to these papers reduces the rate of ink infiltration into the pores and fibers. Understanding and predicting the time scales at which the ink infiltrates the pores and fibers in these coated paper sheets is therefore of great value in the development of inkjet printers. In this study, an existing one-dimensional continuum model utilized for predicting liquid infiltration and subsequent deformations in plain papers is extended to accommodate coated papers. Hereby, the model assumes constant moisture content in the plane of the sheet.

Predictions from the model are compared with experimental results from an immersion and curl test. In the immersion test, a sample is fully immersed in liquid to reveal the time scales for uniform elongation in the plane of the sample due to increasing moisture content through the thickness. The curl test applies a finite amount of liquid to one of the surfaces and measures the resulting curvature over time. Comparison between model predictions and measurement data revealed that the model is able to predict the overall deformation of a sample immersed in demi water. However, for different liquids, the model tends to underestimate the deformation time scales. Additionally, it was found that the coating significantly delays the onset of deformation by acting a barrier with high resistance against flow due to the relatively small pores in the coating. In the curl test on plain paper, model predictions tend to overestimate the resulting maximum curvature compared to the measured data. Furthermore, a discrepancy in the rate of curvature decrease is observed. Comparison of model predictions between the plain and coated paper showed a larger maximum curvature in coated paper sheets.
Finally, results from a parameter study demonstrate that an increase in contact angle, viscosity or coating thickness results in a prolonged duration of liquid infiltration, whereas an increase in pore size or surface tension decreases infiltration times.

Contents

Nomenclature

β	Hygroexpansive coefficient	–
$\chi*$	Reference moisture content	–
χ_E	Moisture content for zero elastic modulus	–
χ_f	Moisture content fibers	–
χ_p	Moisture content pores	–
$\Delta\chi$	Difference moisture content	–
Δt	Time step	s
ΔV	Total volume representative volume element	m^3
ΔV_l	Incremental change in liquid volume	m^3
ΔV_{fl}	Volumetric liquid content fibers	m^3
ΔV_{pl}	Volumetric liquid content pores	m^3
ϵ	Total strain	–
ϵ^e	Elastic strain	–
ϵ^h	Hygroexpansive strain	–
ϵ^p	Plastic strain	–
ϵ_0	Average strain	–
η	Viscosity	$Pa \cdot s$
Γ	Pore-fiber exchange	–
γ	Surface tension	Nm^{-1}
κ	Curvature	m^{-1}
ϕ_f	Fiber storage capacity	–
ϕ_p	Pore porosity	–
σ	Stress	Pa
θ	Contact angle	rad
ζ	Fiber thickness coordinate	m
A	Sheet surface area	m
b	Sheet width	m
c_{perm}	Permeability factor	–
D	Fiber diffusivity	m^2/s
d	Fiber wall thickness	m
E	Elastic modulus	Pa
E_0	Elastic modulus dry fiber	Pa

F	Force	N
H	Sheet thickness	m
K_p	Permeability	m^2
L	Distance from support table	m
L_p	Total accessible pore length	m
M	Moment	Nm
p	Total pressure	Pa
p_c	Capillary pressure	Pa
p_{amb}	Atmospheric pressure	Pa
$p_{c_{max}}$	Maximum capillary pressure	Pa
$p_{c_{min}}$	Minimum capillary pressure	Pa
q	Fiber inflow	m/s
q_f	Vertical fiber flux	m/s
q_p	Vertical pore flux	m/s
R	Curvature radius	m
r	Pore radius	m
r_{max}	Maximum pore radius	m
r_{min}	Minimum pore radius	m
s	Local fiber saturation	–
S_f	Fiber saturation	–
s_f	Average local fiber saturation	–
S_p	Pore saturation	–
t	Time	s
V_f	Total fiber volume	m^3
V_p	Total pore volume	m^3
w	Out-of-plane deformation	m
z	Thickness coordinate	m

1 Introduction

Paper, a porous-fibrous material, exhibits a characteristic behaviour when it interacts with liquids. If the contact angle between the liquid and paper is less than 90 degrees, the liquid starts to infiltrate the porous structure. Initially, it invades the pores and subsequently it diffuses into the fibers. This infiltration causes the fibers to swell over time. This swelling of the fibers can lead to dimensional instability when the paper is subjected to various boundary conditions. Examples of such dimensional instabilities are curling, fluting, and cockling. They are illustrated in Figure 1.1. In modern digital printing systems, water-based inks are replacing toner-based products for sustainability reasons. These water-based inks have a relatively low contact angle with paper. To guarantee dimensional stability during the printing process, special measures in handling the paper sheets are in order due to the liquid absorption of the water-based inks in the paper.

(a) (b) (c)

Figure 1.1: Examples of (a) curling, (b) fluting and (c) cockling [11], [14].

The dimensional instabilities observed when paper becomes wet depend on the underlying microstructure. During the paper manufacturing process, wood fiber pulp is deposited on a moving wire and then dried and pressed in a continuous process to form a wide sheet [14]. The fibers generally lie in the plane of the paper sheet and are most likely to orientate themselves in the direction of motion of the wire. This non-uniform distribution in fiber orientation makes paper an orthotropic material. The mechanical properties of paper are defined in three principal directions: the machine direction (MD), which is defined as the direction of motion during manufacturing, the cross direction (CD), and the thickness direction (z), as illustrated in Figure 1.2. Variations in the mechanical properties in these principal directions contribute to the dimensional instabilities under certain boundary conditions. In this work, these principal directions are used as the main coordinate frame where the height of $z = 0$ refers to the mid plane of the paper sheet.

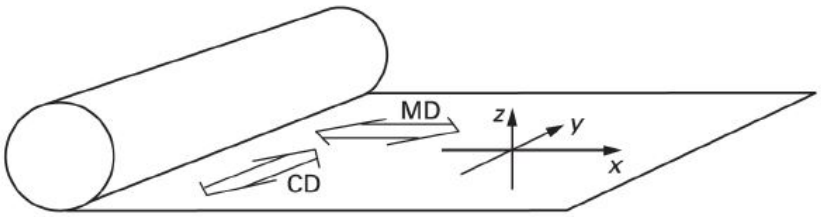

Figure 1.2: Principal directions in paper sheets [14].

At Canon Production Printing, one of the global leaders in digital imaging and industrial printing solutions, research is done on predicting the ink absorption and resulting deformation in paper sheets. TU/e, in collaboration with Canon, has developed a model that can predict the ink ab-

sorption and resulting deformation in a one-dimensional framework for plain paper sheets [4]. The current model employs a simplified representation of the porous network in paper, treating it as a bundle of parallel tubes with different radii. By solving mass conservation equations, the model can predict pore and fiber saturation over time throughout the thickness of the paper sheet. This information, coupled with a simple elastic mechanical model, enables the model to predict paper deformation under varying boundary conditions. While the current model addresses plain paper sheets, this study aims to extend its applicability to coated papers. These papers are coated with a thin polymer layer, which consist of a substantially different pore structure compared to the fibrous material of paper. Consequently, the application of a coating introduces certain qualities such as surface gloss, smoothness, and a reduction in the rate of ink absorption.

Earlier research by Schoelkof et al. [17] exteneded inertial theory to a network model, demonstrating that absorption into a porous network proceeds preferentially through smaller pores. Initially, this process is governed by initial inertial imbibition combined with the exclusion of larger pores due to inertial retardation, followed by the Lucas-Washburn absorption dynamics. This inertially driven selectivity establishes a preferred pathway through the smaller pores during sequential filling. Yin et al. [21] developed a pore network model for primary imbibition and applied it to simulate droplet penetration into the coating layer of a coated paper. Results obtained from the simulation showed a linear decrease in droplet volume with time, which contradicts the expected $\sqrt{t}$-behaviour in vertical imbibition that is obtained using macroscopic single phase Darcy's law. The study suggested that the constant imbibition rate is likely due to the wetting phase encountering more viscous resistance and greater accessibility of pores for liquid penetration. A suggestion was made to switch to the Richards equation to model liquid imbibition in the coated layer of a coated paper. Alleborn et al. [2], investigated the spreading and sorption of droplets on an unsaturated coating substrate. They employed the Richards equation to model unsaturated flow in the coating layer, coupled with droplet dynamics described by lubrication approximation. Numerical results showed that a steep capillary sorption curve leads to a sharp localization of liquid infilitration. Van der Sman [18], developed a model that can describe the deformation of paper sheets subjected to changes in moisture content. The model assumed that the moisture content changes in the plane of the sheet but remains constant through the thickness. It was found that in the wet state, the developed model accurately captures the qualitative behaviour of paper observed in experiments. This led to the conclusion that the inhomogeneous moisture content in the plane contributes to the out-of-plane deformations of wetted paper sheets.

The goal of this study is to understand the physics behind the through thickness liquid transport in coated paper sheets and the subsequent mechanical deformations. The objective is to extend the current model from Dave et al. [4], so it can predict the time scales at which liquid flows through coating and paper pores, and makes the fibers swell. Experimental measurements on wetted paper strips, both in- and out-of-plane, will be used to validate the model. Different inputs will be explored with the validated model to study their effect of on liquid transport and sheet deformation.

The report is structured as follows. First the essential constitutive equations for both the liquid transport and mechanical model are presented in Chapter 2. A general representation of the underlying theory is given. At the end of this Chapter the theory is more specialized towards coated paper sheets by discussing boundary and interface conditions. Chapter 3 outlines the numerical implementation of these equations, while Chapter 4 gives a short description on the experimental methods used for validation. Parameters that are used in the model are discussed in Chapter 5. Predictions made by the model are compared with experimental results in Chapter 6, along with a parameter study. Chapter 7 provides concluding remarks summarizing the key findings of the study. Finally, Chapter 8 discusses the limitations of the model and possibilities for future research are offered.

2 Theoretical Background

In order to make predictions on moisture-induced deformations in (coated) paper sheets, a model describing the liquid transport into the paper sheet coupled with a mechanical model describing the resulting deformation is developed. The model primarily builds upon N. Dave's framework [4], which characterizes the liquid absorption and resulting deformation on the continuum level, i.e., the sheet scale. In order to represent the processes at the micro-scale realistically in an average sense, he employed insights obtained from highly idealized models defined at the microstructure scale. For simplicity reasons, he assumed that the water transport solely depends on the thickness direction z and time t. This means that the transport is assumed to be uniform along the in-plane directions of the medium. This work adopts a similar one-dimensional continuum model approach, with some minor adjustments to the idealized micro-scale models. Although most of the model's core principles remained the same, a different solution technique is employed.
In this chapter, the theoretical background information used to model the physical processes is explained. Alterations made to the modeling philosophy from N. Dave's work are highlighted and included with an explanation for the suggested modifications. First, details about the liquid transport are given, followed by an overview of the mechanical model. Finally, the boundary and interface conditions are discussed.

2.1 Liquid transport

The liquid transport model aims to predict the amount of liquid in the porous medium and fibers over time. In a one-dimensional continuum model, it is easier to determine this amount in terms of volume fractions. Multiple volume fractions are defined and used in the model. First, the volume fractions that describe the volumetric liquid content in the pores V_{pl} and fibers V_{fl}. These fractions represent the ratio of liquid volume within a small representative volume element of the micro-structure to the total volume of that element ΔV. They are denoted by χ_p and χ_f respectively,

$$\chi_p = \frac{\Delta V_{pl}}{\Delta V}; \qquad \chi_f = \frac{\Delta V_{fl}}{\Delta V}. \tag{2.1}$$

Secondly, the sheet's porosity and the fibers' storage capacity. These volume fractions describe the total amount of liquid that can be stored relative to their respective volumes,

$$\phi_p = \frac{\Delta V_p}{\Delta V}; \qquad \phi_f = \frac{\Delta V_{fp}}{\Delta V_f} \tag{2.2}$$

where ΔV_p is the volume of pore space contained in the representative volume element ΔV. The total volume of fibers in the representative volume element is denoted by ΔV_f and equals $\Delta V - \Delta V_p$. These fibers can store a maximum amount of liquid, which is denoted by ΔV_{fp}.
The latter volume fractions can be combined to give the saturation of the pores and fibers. These volume fractions describe the volumetric scaled liquid content within the representative volume element in the pores and fibers, respectively. The saturation ranges from zero to one, where zero saturation is equivalent to a dry state, and a saturation of one is equivalent to a fully wet state. The pore and fiber saturation are given by,

$$S_p = \frac{\chi_p}{\phi_p}; \qquad S_f = \frac{\chi_f}{\phi_f(1-\phi_p)}. \tag{2.3}$$

The model uses saturation as a variable to express the amount of liquid in the pores and fibers at a height z, evaluated at a certain moment in time t. Therefore, saturation is expressed as a function of both space and time.

The liquid transport model describes the physical process of a liquid entering the porous network (driven solely by capillary suction) and the subsequent transport through the walls of the pores into the fibers. The model can thus be split into two parts, which characterize the wetting of

the pore network and the wetting of the fibers, respectively. This is schematically depicted in Figure 2.1.
Wetting of the pore network is described by a one-dimensional unsaturated flow model that describes the change in saturation over time through the thickness. The governing equation behind this unsaturated flow model is called the classical Richards equation [16]. The equation is obtained by applying mass conservation and Darcy's flow law. The Richards equation alone does not consider the exchange between the pore network and fibers. An exchange term is added to the classical Richards equation to account for this and ensure the mass in the whole system is conserved. Via this exchange term, the expression is coupled to a second equation describing the liquid transport into the fibers derived from a one-dimensional diffusion equation. The combination of these equations thus encapsulates the dynamics of liquid transport in the paper sheet,

$$\phi_p \frac{\partial S_p}{\partial t} + \frac{\partial}{\partial z}\Big(\frac{K_p(S_p)}{\eta}\frac{\partial p_c(S_p)}{\partial z}\Big) + \Gamma(S_p, S_f) = 0 \tag{2.4a}$$

$$\phi_f \frac{\partial S_f}{\partial t} + \frac{\partial q_f}{\partial z} - \Gamma(S_p, S_f) = 0 \tag{2.4b}$$

where p_c, μ, K_p, and Γ are the capillary pressure, dynamic viscosity, permeability, and exchange term, respectively. The first two terms in Equation 2.4a come from the classical Richards equation; a complete derivation of this equation can be found in Appendix A. It is clear from this equation that the gradient of the capillary pressure drives the liquid transport in the pore network. As we assume that the volumetric flux from the pore transport through the thickness is much faster than that from the fiber phase, the variable q_f can be neglected. Inflow into the fibers is thus only possible through local exchange between pores and adjacent fibers.

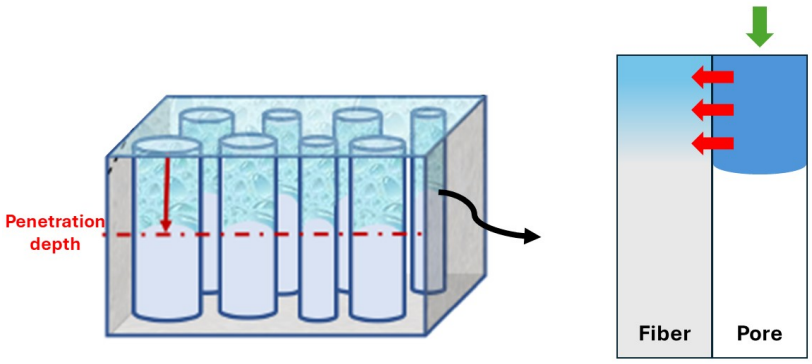

Figure 2.1: Schematic of liquid transport model [4].

2.2 Unsaturated flow in porous media

The variables capillary pressure, saturation and permeability from the unsaturated flow description are related. In literature, formulations such as Brooks-Corey [3] and van Genuchten [8] are widely used to describe these relations. These formulations find their origin in the geomechanics community, where they are widely used in research on unsaturated flow through soils. Dave's work uses a formulation based on the measured pore size distribution. Throughout the remainder of this work, the Dave's modelling framework is used with a slight extension to describe the fully saturated zone for a larger pressure range. Here, a brief overview of this model is given and compared with the Brooks-Corey and van Genuchten model. A brief description of these two models can be found in Appendix C.

2.2.1 Pore size distribution

The pore size distribution $P(r)$ is the probability that a specific pore with radius r is encountered in a porous medium. It can be coupled to the wetted pore volume with the following expression,

$$V_{pl} = L_p \int_0^r P(\rho)\pi\rho^2 d\rho \tag{2.5}$$

where L_p is the total accessible pore length, which is assumed to be independent of r. There is no direct experimental access to $P(r)$. However, using a mercury intrusion porosimetry (MIP) test, some information can be obtained about the distribution [10]. An MIP test uses a liquid with a contact angle higher than 90 degrees, such as mercury. Such liquids do not penetrate the porous medium by itself. Instead, an external pressure is needed. The intruded volume is then measured as a function of this applied external pressure. With the use of the Young-Laplace equation in a cylindrical tube, an estimate for the pore radius can then be determined,

$$r = \frac{2\gamma cos(\theta)}{p_c} \tag{2.6}$$

here γ represents the surface tension and θ the contact angle.
The outcome of an MIP test reveals a relationship between pore radius and saturation. The following equation is used to extract the pore size distribution from a MIP test,

$$P(r) = \frac{V_p}{L_p \pi r^2}\frac{dS_p}{dr} = \frac{V_p}{L_p \pi r^2} f(r). \tag{2.7}$$

The full derivation for this equation is given in Appendix B. The unknown parameter L_p can be obtained by applying the normalization condition, $\int_0^\infty P(r)dr = 1$.

2.2.2 Water retention curves

The relationship between the capillary pressure and saturation is commonly referred to as the water retention curve. Here, the saturation is formulated as a function of capillary pressure. In the work of Dave et al. [4], the relation between saturation and capillary pressure is derived from the results of the MIP experiments by fitting a piece-wise linear approximation to the measured saturation,

$$S_p(r) = \frac{r - r_{min}}{r_{max} - r_{min}} \tag{2.8}$$

where r_{min} and r_{max} refer to the minimum and maximum fitted pore sizes respectively. They are the derived by fitting Equation 2.8 to the linear part of the measured water retention curve. By substituting Equation 2.6 for the pore radius r, a function for the water retention curve can be derived,

$$S_p(p_c) = \frac{\frac{p_{c_{max}}}{p_c} - 1}{\frac{p_{c_{max}}}{p_{c_{min}}} - 1} \qquad p_{c_{min}} \leq p_c \leq p_{c_{max}} \tag{2.9}$$

where $p_{c_{min}}$ and $p_{c_{max}}$ are the capillary pressures corresponding to the maximum and minimum pore radius respectively. The relation is only valid on the domain ranging from the minimum to the maximum capillary pressure. However, the function needs to be defined for all values of p_c. This is done by specifying that the saturation is equal to one for capillary pressures lower than $p_{c_{min}}$ and equal to zero for capillary pressures higher than $p_{c_{max}}$,

$$S_p(p_c) = \begin{cases} 1 & p_c < p_{c_{min}} \\ \frac{\frac{p_{c_{max}}}{p_c} - 1}{\frac{p_{c_{max}}}{p_{c_{min}}} - 1} & p_{c_{min}} \leq p_c \leq p_{c_{max}} \\ 0 & p_c > p_{c_{max}}. \end{cases} \tag{2.10}$$

The piece-wise linear approximated model (linear model), Brooks-Corey model (BC model) and van Genuchten model (VG model) are compared with each other in Figure 2.2a. Derivation of the parameters used in the models can be found in Appendix C.

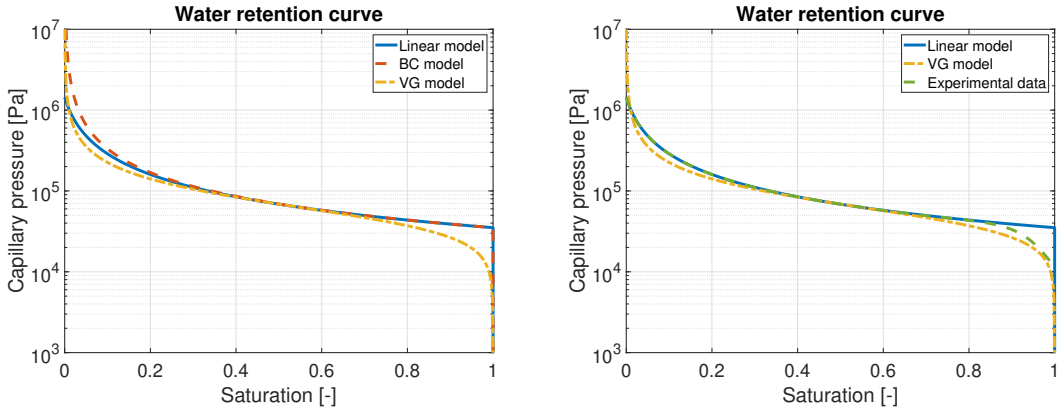

(a) Comparison between models.

(b) Comparison with experiment.

Figure 2.2: Water retention curve: models and experiments.

The linear approximated model and Brooks-Corey model show similar behavior. At zero saturation, however, the Brooks-Corey relation goes to infinity. The van Genuchten model shows this same behavior for zero saturation. In Figure 2.2b, the linear and van Genuchten models are compared with the results from the MIP test. For low saturation, the linear approximation is in agreement with the measurements. For high saturation, the measured capillary pressure lies in between the predicted values of the linear and van Genuchten models.

2.2.3 Permeability

The permeability is a measure of the resistance against flow in a porous medium. A low permeability means a high resistance against flow, which leads to larger timescales at which a specific volume of liquid can move through the medium. The permeability is not constant in an unsaturated porous medium because unfilled pores cannot transmit any liquid. As more pores get filled with liquid, the permeability of the medium increases. This continues until all pores are filled and the maximum permeability is reached. A model that can accurately describe the relation between saturation and permeability is thus of vital importance to model the liquid penetration in unsaturated porous media.

Paper has a complex structure of pores connected by throats with different lengths and radii. It is possible to develop a relation between saturation and permeability using numerical models describing this complex three-dimensional structure [15], [20]. However, this takes much computation time and is impossible in one dimension. The liquid transport model from the work of N. Dave et al. [4] simplifies this complex structure by assuming flow through a porous rectangular block via N cylindrical-shaped pores, as shown in Figure 2.1. With the assumption of N parallel tubes, it is possible to formulate three tube models [10]: identical cylinders, cylinders with different radii, and identical cylinders with different radii along their length. These three models are visually depicted in Figure 2.3.

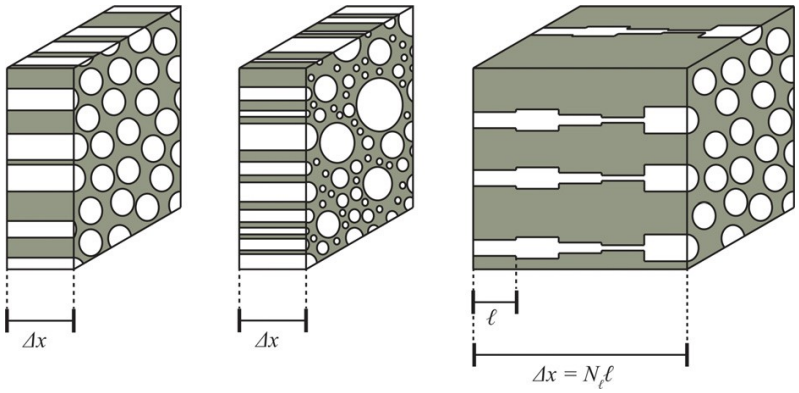

Figure 2.3: Three different parallel tube models: 1. identical cylinders (left), 2. cylinders with different radii (middle) and 3. identical cylinders with different radii along it length (right) [10].

The second and third tube models strongly indicate the upper and lower bounds of the permeability in the three-dimensional structure. These bounds are, however, a factor of 100 to 1000 apart. The actual permeability lies thus somewhere in between these values. The second tube model, which over-predicts the permeability, is scaled with a constant factor to account for this. The one-dimensional flux q_p through the thickness of the porous block can, in this case, be written according to the Hagen-Poiseuille equation,

$$q_p = -\sum_{i=1}^{N} \frac{\pi r_i^4}{8\eta A} \frac{dp}{dz}. \tag{2.11}$$

By using the definition of the pore porosity, Equation 2.2, and writing the flux as a Darcy equation, the permeability can be expressed as,

$$K_p = \frac{1}{8}\phi_p \frac{\int_0^r P(\rho)\rho^4 d\rho}{\int_0^\infty P(r)r^2 dr}. \tag{2.12}$$

Solving the integrals leads to a relation for the permeability dependent on r. Rewriting Equation 2.8 and substituting for r gives a relation that is dependent on the saturation. The saturation can be expressed as a function of the capillary pressure (Equation 2.10), meaning that the permeability is thus indirectly dependent on the capillary pressure. Here, the expression is given as a function of saturation, as this is the one that is used in the model,

$$K_p(S_p) = \frac{\phi_p}{24 c_{perm}} \frac{\big(r_{min} + S_p(r_{max} - r_{min})\big)^3 - r_{min}^3}{r_{max} - r_{min}} \tag{2.13}$$

where c_{perm} is the scaled permeability factor and is set equal to 600. A full derivation of this expression can be found in Appendix D. The resulting relation between permeability and saturation is plotted in Figure 2.4. In the pore network, the empty pores cannot transmit liquid. The small pores are assumed to fill first due to higher capillary suction [2] and lower inertia effects [17]. These pores have a much larger resistance against flow with respect to the larger pores. This explains the slow increase for low saturation in Figure 2.4. As the saturation increases, the larger pores start to fill, rapidly increasing permeability as the resistance against flow in these pores is much lower.
Figure 2.4 also shows the permeability model proposed by van Genuchten [8]. Similar to the linear model, it shows an initial slow increase followed by a rapid increase in permeability with increasing saturation. Nonetheless, the van Genuchten model predicts an overall slower increase to maximum permeability than the linear model. A full description on the van Genuchten permeability function is given in Appendix D.

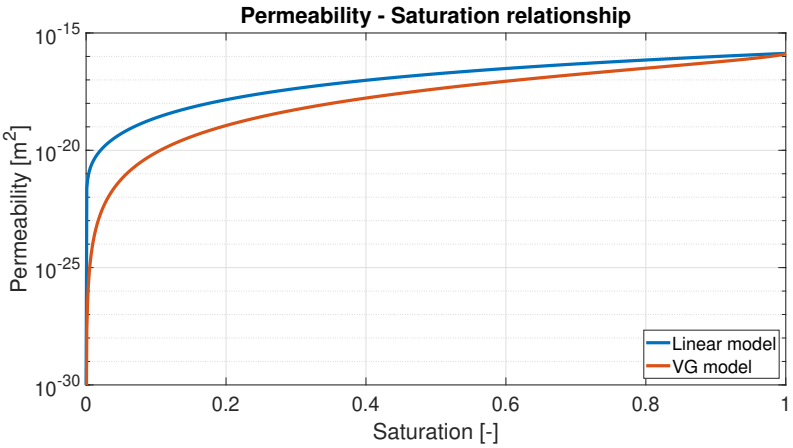

Figure 2.4: Relationship between permeability and saturation used in this work.

2.3 Pore-fiber mass exchange

To describe the liquid transport from the pores into the fibers a relation for the exchange term Γ is established. When water enters the pores, the surface of the surrounding fibers becomes wet. From the surface the water travels through the thickness of the fiber wall, leading to an increase in saturation of the fiber. In this work, it is assumed that this motion through the fiber wall can be expressed as a one-dimensional diffusion process. Additionally, it is assumed that both sides of the fiber experience the same step change from local fiber saturation $s = 0$ to $s = 1$ when the water gets in contact with the fiber wall. The local fiber saturation is the saturation in a small representative volume element ΔV_f of the fiber. The lumen, located at the fiber's center, is assumed to be closed. Therefore, the fiber thickness equals twice the fiber wall thickness d, as shown in Figure 2.5

A symmetry condition is applied because both sides of the fiber experience the same step change. So, in the formulation of the one-dimensional diffusion equation, only half the fiber thickness is used. The one-dimensional diffusion equation looks as follows,

$$\phi_f \frac{\partial s}{\partial t} = D \frac{\partial^2 s}{\partial \zeta^2} \tag{2.14}$$

where D and ζ represent the constant fiber diffusivity and fiber thickness direction respectively.

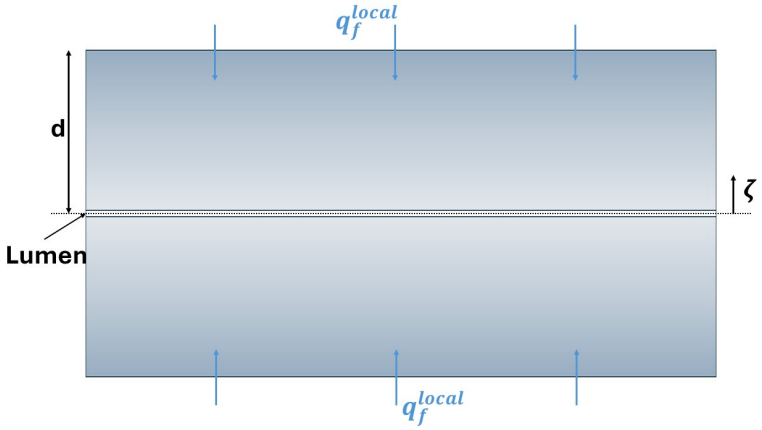

Figure 2.5: Schematic for liquid diffusion into the fiber.

The boundary and initial conditions are,

$$\frac{\partial s}{\partial \zeta}(0,t) = 0 \tag{2.14a}$$

$$s(d,t) = 1 \tag{2.14b}$$

$$s(\zeta,0) = 0. \tag{2.14c}$$

The analytical solution to the diffusion equation is given in terms of a Fourier series,

$$s(\zeta,t) = 1 - \frac{4}{\pi}\sum_{n=0}^{\infty}\frac{(-1)^n}{2n+1}e^{-\frac{D}{\phi_f}\left(\frac{(2n+1)\pi}{2d}\right)^2 t}cos\left(\frac{(2n+1)\pi}{2d}\zeta\right). \tag{2.15}$$

This equation describes the local fiber saturation through the thickness of the fiber. Taking the average of this and dividing by the fiber thickness gives an estimate on the local amount of fluid in the fiber,

$$s_f(t) = \frac{\int_0^d s(\zeta,t)d\zeta}{d}. \tag{2.16}$$

Equation 2.15 can also be used to find an expression for the inflow at the surface of the fiber. This is done by evaluating the following equation,

$$q(d,t) = D\frac{\partial s}{\partial \zeta}(d,t). \tag{2.17}$$

The solution for the local fiber saturation as a function of time and inflow are plotted in Figure 2.6a and Figure 2.6b respectively. The solutions are based on 1000 Fourier terms. It can be observed that the relation between saturation and inflow behaves as a combination of a linear and power law relationship. The inflow can then be expressed as a function of the saturation by the following analytical equation,

$$q_f(s_f) = \frac{D}{d}\left(a(1-s_f) + b(\frac{1}{s_f} - 1)\right) \tag{2.18}$$

where a and b are values that are fitted to the solution from the Fourier series. For the values of $a = 1.45$ and $b = 0.6$ a good fit is observed, as shown in Figure 2.6b by the dashed line.

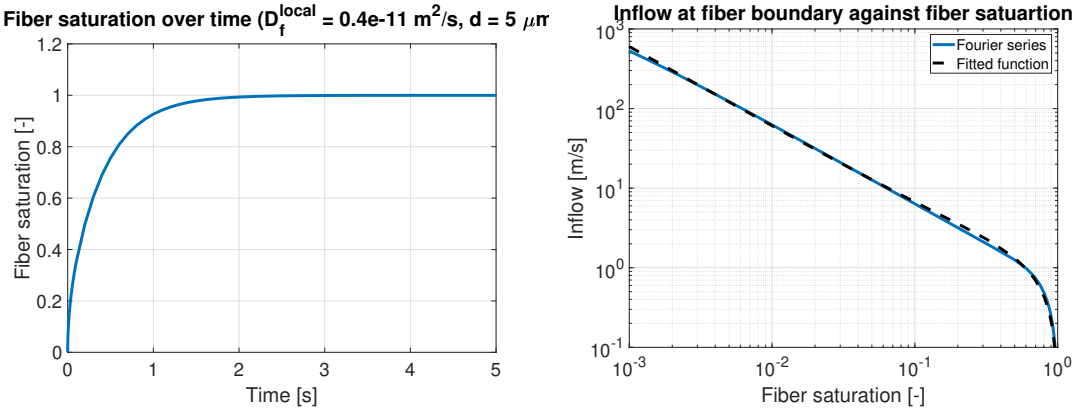

(a) Fiber saturation as a function of time.

(b) Fiber saturation as a function of inflow.

Figure 2.6: Relations for fiber saturation.

The local fiber saturation only describes the liquid content in a small region around a specific pore. It thus only gives information on the saturation of a small fraction of the total fiber volume.

To transform to a global saturation, a summation of all the local volumetric liquid contributions needs to be performed and divided by the total liquid storage of the fibers,

$$\phi_f S_f = \frac{\sum_{i=1}^{N_w} \Delta A_i \int_0^t q_f dt}{V_f} \tag{2.19}$$

here ΔA_i is the wetted surface area through which diffusion happens for a specific pore and N_w is the number of saturated pores. Simplifying the summation like this is allowed because the boundary flux q_f for an unsaturated, empty pore equals zero. So, only saturated pores contribute to the filling of the fibers. Assuming that these saturated pores fill at the same rate and taking the time derivative in Equation 2.19 leads to an expression for the pore-fiber mass exchange term,

$$\Gamma = \frac{\sum_{i=1}^{N_w} \Delta A_i}{V_f} q_f(S_f). \tag{2.20}$$

In this expression the ratio of wetted surface area to the fiber volume can be written as,

$$\frac{\sum_{i=1}^{N_w} \Delta A_i}{V_f} = \frac{\ln\left(1 + S_p \frac{r_{max} - r_{min}}{r_{min}}\right)}{\ln\left(\frac{r_{max}}{r_{min}}\right) d}. \tag{2.21}$$

A full derivation of this equation is given in Appendix E.

2.4 Mechanical deformation

The water uptake by the fibers results in swelling, which drives the mechanical deformation of the paper sheet. A one-dimensional hygro-mechanical model is used to predict the deformation resulting from an immersion and curl test. As only one dimension is considered, the total predicted strain is in the plane of the sheet, whereas the predicted curvature for the curl test is out-of-plane. This model subdivides the total strain into three components: the elastic ϵ^e, plastic ϵ^p and hygroexpansive strain ϵ^h. A schematic representation of this is given in Figure 2.7. The summation of these three terms gives the total strain,

$$\epsilon = \epsilon^e + \epsilon^p + \epsilon^h. \tag{2.22}$$

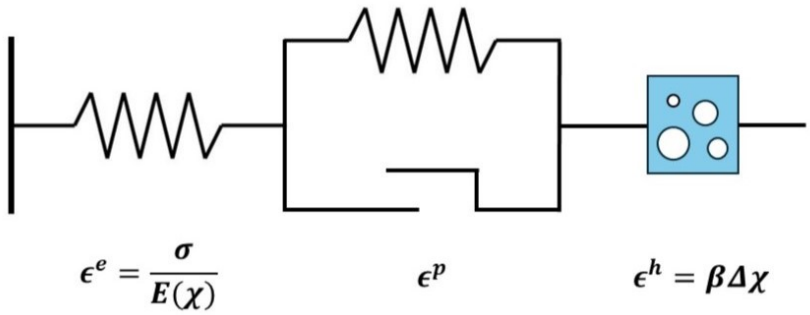

Figure 2.7: Schematic mechanical model.

The hygroexpansive strain describes the swelling of the fibers due to an increase in moisture content and can be written as,

$$\epsilon^h = \beta \Delta \chi = \beta \phi_f S_f \tag{2.23}$$

where β denotes the hygroexpansive coefficient and $\Delta\chi = \chi - \chi^*$ is the difference between the current and reference moisture content in the paper [14]. This reference moisture content can be

chosen freely, where the hygroexpansive strain is defined to be zero at $\chi = \chi^*$. The change in moisture content is related to the saturation of the fibers and can be given as the product of the storage capacity of the fibers ϕ_f and saturation S_f.

The elastic strain is linearly dependent on the stress in the material and is described by Hooke's law as,

$$\epsilon^e = \frac{\sigma}{E(\chi)} \tag{2.24}$$

where σ is the stress and $E(\chi)$ is the elastic modulus, which is dependent on the moisture content. An increase in fiber saturation leads to a decrease in the elastic modulus. It is assumed that this relation is linear and given as,

$$E(\chi) = E_0(1 - \frac{\chi}{\chi_E}) \tag{2.25}$$

where E_0 is the elastic modulus related to a dry fiber, i.e., zero moisture content [18]. The constant χ_E denotes the moisture content for which the elastic modulus equals zero.

Considering static equilibrium, the forces and moments in the paper sheet should be balanced. This work assumes no external forces or moments are applied to the paper sheet. This means that the internal forces and moments should be balanced, meaning that the following two equilibrium equations hold,

$$F = \int_{-\frac{H}{2}}^{\frac{H}{2}} \sigma b dz = 0 \tag{2.26}$$

$$M = \int_{-\frac{H}{2}}^{\frac{H}{2}} \sigma b z dz = 0 \tag{2.27}$$

where H and b represent the height and width of the paper sheet, respectively [6]. Additionally, the total strain contribution can be expressed in terms of the average strain and curvature,

$$\epsilon = \epsilon_0 - \kappa z \tag{2.28}$$

where ϵ_0 is the average strain, which is equal to the strain of the midplane of the sheet, and κ the curvature. Combining this with Equation 2.22 gives the following expression for the elastic strain,

$$\epsilon^e = \epsilon_0 - \kappa z - \epsilon^p - \epsilon^h. \tag{2.29}$$

The equilibrium equations can then be written in terms of the average strain and curvature by substituting Equation 2.24 in combination with Equation 2.29. This gives the following result:

$$\int_{-\frac{H}{2}}^{\frac{H}{2}} E(\chi)(\epsilon_0 - \kappa z - \epsilon^p - \epsilon^h) b dz = 0 \tag{2.30}$$

$$\int_{-\frac{H}{2}}^{\frac{H}{2}} E(\chi)(\epsilon_0 - \kappa z - \epsilon^p - \epsilon^h) b z dz = 0. \tag{2.31}$$

These two equations can be used to determine the values of the average strain and curvature when the moisture content through the thickness of the paper sheet is known. Solving for average strain and curvature is most easily done by writing the two equations into one system of equations,

$$\begin{vmatrix} A & -B \\ -B & D \end{vmatrix} \begin{vmatrix} \epsilon_0 \\ \kappa \end{vmatrix} = \begin{vmatrix} F_\alpha \\ M_\alpha \end{vmatrix} \tag{2.32}$$

with,

$$A = \int_{-\frac{H}{2}}^{\frac{H}{2}} E(\chi) b dz \tag{2.33}$$

$$B = \int_{-\frac{H}{2}}^{\frac{H}{2}} E(\chi) b z dz \tag{2.34}$$

$$D = \int_{-\frac{H}{2}}^{\frac{H}{2}} E(\chi) b z^2 dz \tag{2.35}$$

$$F_\alpha = \int_{-\frac{H}{2}}^{\frac{H}{2}} E(\chi)\left(\epsilon^p - \epsilon^h\right) b dz \tag{2.36}$$

$$M_\alpha = \int_{-\frac{H}{2}}^{\frac{H}{2}} E(\chi)\left(\epsilon^p - \epsilon^h\right) b z dz. \tag{2.37}$$

The parameter b can be taken outside the integral when considering a constant width. The elastic modulus and hygroexpansive strain are a function of the moisture content, which varies through the thickness of the paper sheet. This means that both variables cannot be taken outside the integral. This work assumes that there is no plastic strain, meaning that the force and moment integrals only depend on the hygroexpansive strain. The integrals can be determined for a given moisture content, and the system can be solved to find values for the average strain and curvature.

2.5 Boundary and interface conditions

The liquid transport model, described at the beginning of this chapter, is a general representation of a porous medium that exchanges liquid with surrounding bulk material. When considering a (coated) paper sheet under certain circumstances, appropriate inputs and boundary conditions must be given to specify the model for its use case. This work considers two use cases: an immersion and a curvature test. These use cases resemble experimental setups, further described in section 4. Here, a short generic overview of the boundary conditions is given alongside a description of the interface conditions. The specific boundary conditions for the immersion and curl test are mentioned in section 4. In all cases an initially dry sheet is considered. This initial condition used to described this is a constant value of the medium's minimum capillary pressure through the whole thickness, as this relates to zero pore saturation.

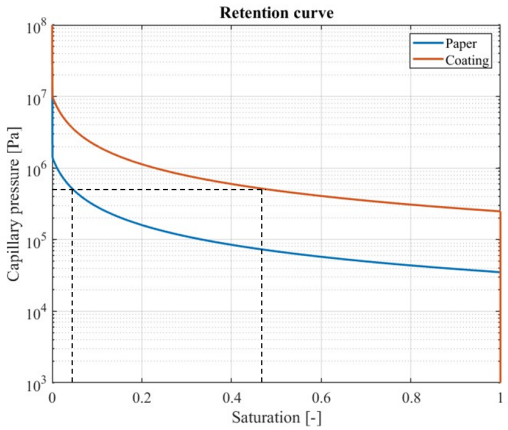

Figure 2.8: Visualization of discontinuity in pore saturation between coating and paper for constant capillary pressure.

A coated paper sheet can be modeled as a layered stack of two porous media. Before specifying the boundary conditions, it is interesting to analyze the interface condition between these two layered stacks. The coating and paper sheet have a different pore size distribution because their respective pore network differs. As a result, the saturation inside the pore networks may be different for a specific capillary pressure, as illustrated in Figure 2.8. As the pressure is continuous through the

whole thickness of the paper sheet, a discontinuity in saturation can exist at the interface. A technique that is commonly used in modeling layered porous media is to solve Equation 2.4 for capillary pressure because then the condition at the interface implies continuity of the primary dependent variable, which is provided naturally by a (continuous) finite element interpolation [9]. This solution strategy differs significantly from the one used by Dave, as he solved for the saturation. In this work, the liquid transport model is solved for capillary pressure, which significantly increases the ease of solving the equation. The boundary conditions are thus also specified in capillary pressure instead of saturation. Additionally, at the interface there should be a continuity in liquid flow. The amount of liquid that leaves the coating should enter the pores of the paper. The discretization of the weak form of the Richards equation takes care of this continuity.

Applying a liquid to a paper sheet leads to full saturation of the surface where the liquid is applied. In the model framework this is equivalent to prescribing a pore saturation of one to the specified boundary where the liquid is applied. However, from Equation 2.10 it is evident that the pore saturation equals one for all capillary pressure lower than the minimum capillary pressure of the medium. This thus leaves a question on which capillary pressure must be specified at the boundary. To answer this the total pressure at the boundary is considered, which is given by,

$$p = p_{amb} - p_c \tag{2.38}$$

where p and p_{amb} are the total and atmospheric pressure respectively. The total pressure at the surface of the paper sheet is equal to the atmospheric pressure. From Equation 2.38, it then follows that the capillary pressure should be equal to zero, which also relates to a pore saturation of one. Liquid application on the top or bottom of the paper sheet is thus given by,

$$p_c(\pm\frac{H}{2}, t) = 0 \tag{2.39}$$

where a value of $+\frac{H}{2}$ refers to the top of the paper sheet and a value of $-\frac{H}{2}$ to the bottom. Additionally, it is useful to prescribe a no flow condition on the boundaries. The flow is driven by a pressure difference through the sheet thickness. A pressure difference of zero thus results in no flow, which means that this boundary term can be written as,

$$\frac{\partial p_c}{\partial z}(Z, t) = 0 \tag{2.40}$$

where Z refers to an arbitrary boundary.

3 Numerical implementation

Due to the non-linearity of the liquid transport model, numerical tools are implemented for finding a solution. In this work an implicit finite difference method is used for discretization in time. Besides that, a Finite Element framework is established for discrization in space. By combining the two methods it is possible to find solutions for the dependent variables over time. To solve the pore-fiber mass exchange it is straightforward to take the fiber saturation as the dependent variable. As already discussed in Chapter 2.5 the unsaturated flow description will be solved for the capillary pressure, as this is beneficial in the implementation of the interface condition. A disadvantage of choosing the capillary pressure as primary dependent variable is that it can produce significant global mass balance errors under certain saturation conditions unless very small time steps are used in the numerical approach [5]. This error is clearly visible in the work of Gottardi [9], where multiple solution techniques are compared with respect to each other. It is important to take these mass balance errors into account when determining the time step for the numerical simulation. The liquid transport model from Equation 2.4 is thus rewritten in terms of capillary pressure. This results in the following two equations that will be solved with the use of the numerical model,

$$\phi_p \frac{\partial S_p(p_c)}{\partial t} + \frac{\partial}{\partial z}\Big(\frac{K_p(p_c)}{\eta}\frac{\partial p_c}{\partial z}\Big) + \Gamma(p_c, S_f) = 0 \tag{3.1a}$$

$$\phi_f \frac{\partial S_f}{\partial t} - \Gamma(p_c, S_f) = 0. \tag{3.1b}$$

3.1 Time discretization

The two primary dependent variables, capillary pressure and fiber saturation, both vary over time. In this work, the implicit backward Euler finite difference technique is used to discretize the system in small time steps ($t^n = n\Delta t$). Using the backward Euler method, the time derivative at the next time step (t^{n+1}) is approximated by using the values of the unknown function at the next time step. Applying the backward Euler method on the liquid transport model results in,

$$\phi_p \frac{S_p(p_c) - S_p(p_{c,0})}{\Delta t} + \frac{d}{dz}\Big(\frac{K_p(p_c)}{\eta}\frac{dp_c}{dz}\Big) + \Gamma(p_c, S_f) = 0 \tag{3.2a}$$

$$\phi_f \frac{S_f - S_{f,0}}{\Delta t} - \Gamma(p_c, S_f) = 0. \tag{3.2b}$$

Here the subscript refers to the evaluated time step, i.e. $p_{c,0} = p_c(z, t^n)$ and $p_c = p_c(z, t^{(n+1)})$. The same principle applies to the fiber saturation.

3.2 Spatial discretization

The thickness direction of the paper sheet is discretized with the use of the Finite Element Method. This is done by subdividing the paper sheet in small elements, which are connected by nodes. On each element the solution is approximated by a polynomial. The approximation of the exact solution on the whole domain can be written as,

$$p_c^h(z, t^n) = \sum_{i=1}^{N_{nodes}} N_i(z) p_{c,i}(t^n) \tag{3.3a}$$

$$S_f^h(z, t^n) = \sum_{i=1}^{N_{nodes}} N_i(z) S_{f,i}(t^n). \tag{3.3b}$$

Here p_c^h and S_f^h refer to the approximations of the solution for the capillary pressure and fiber saturation respectively. The shape function associated with node i is denoted by $N_i(z)$, with nodal

values given by $p_{c,i}$ and $S_{f,i}$. The summation is taken over the total number of nodes N_{nodes}. While it is possible to solve Equation 3.2b independently in each node without the use of the Finite Element method, opting for a Finite Element approach is preferred. This choice allows for the interconnection of the solution at each nodes through the use of shape functions, resulting in faster convergence of the solution.
So to find an approximation of the exact solution the nodal values need to be determined. To estimate these values with the use of the Finite Element method, first the time discretized differential equations, Equation 3.2a and Equation 3.2b, are each cast in a weak form,

$$\int_{-\frac{H}{2}}^{\frac{H}{2}} v(z)\phi_p\big(S_p(p_c) - S_p(p_{c,0})\big)dz - \int_{-\frac{H}{2}}^{\frac{H}{2}} \frac{dv}{dz}\Delta t\frac{K_p(p_c)}{\eta}\frac{dp_c}{dz}dz + \int_{-\frac{H}{2}}^{\frac{H}{2}} v(z)\Delta t\Gamma(p_c, S_f)dz + v(z)\Delta t\frac{K_p(p_c)}{\eta}\frac{dp_c}{dz}\Big|_{-\frac{H}{2}}^{\frac{H}{2}} = 0 \qquad \forall\, v(z) \tag{3.4a}$$

$$\int_{-\frac{H}{2}}^{\frac{H}{2}} w(z)\phi_f(1-\phi_p)\big(S_f - S_{f,0}\big)dz - \int_{-\frac{H}{2}}^{\frac{H}{2}} w(z)\Delta t\Gamma(p_c, S_f)dz = 0 \qquad \forall\, w(z). \tag{3.4b}$$

In these equations H is the thickness of the paper sheet and $v(z)$ and $w(z)$ the weight functions. The next step is to substitute the approximate solutions for the exact solutions in the weak forms. For convenience the approximate solutions are written in matrix form, storing the nodal values and shape functions in column matrices. Galerkin's method is used for discretization of the weight functions, which requires that the weight functions are of the same form as the approximate solutions. For both approximate solutions linear shape functions are used, so the weight functions also use a linear shape function. Substituting the approximate expressions leads to the following discretized system,

$$\begin{aligned} \boldsymbol{r_1} + \boldsymbol{q} &= \boldsymbol{0} \\ \boldsymbol{r_2} &= \boldsymbol{0} \end{aligned} \tag{3.5}$$

with,

$$\boldsymbol{r_1} = \int_{-\frac{H}{2}}^{\frac{H}{2}} \Big(\boldsymbol{N}(z)\big[\phi_p\big(S_p(p_c^h) - S_p(p_{c,0}^h)\big) + \Delta t\Gamma(p_c^h, S_f^h)\big] - \frac{d\boldsymbol{N}}{dz}\Delta t\frac{K_p(p_c^h)}{\eta}\frac{dp_c^h}{dz}\Big)dz \tag{3.5a}$$

$$\boldsymbol{r_2} = \int_{-\frac{H}{2}}^{\frac{H}{2}} \boldsymbol{N}(z)\Big(\phi_f(1-\phi_p)\big(S_f^h - S_{f,0}^h\big) - \Delta t\Gamma(p_c^h, S_f^h)\Big)dz \tag{3.5b}$$

$$\boldsymbol{q} = \boldsymbol{N}(z)\Delta t\frac{K_p(p_c^h)}{\eta}\frac{dp_c^h}{dz}\Big|_{-\frac{H}{2}}^{\frac{H}{2}} \tag{3.5c}$$

here the weak form from Equation 3.3a is split in two parts, a residual term $\boldsymbol{r_1}$ and a boundary term $\boldsymbol{q}$, as it is easier to work with a separate boundary term in the software implementation of the Finite Element framework. The second weak from does not have any boundary terms, so in this case all terms are placed in the residual $\boldsymbol{r_2}$.

3.3 Linearization

The discretized system from Equation 3.5 is highly non-linear due to the non-linear relations p_c-S_p and p_c-K_p. To solve this non-linear set of algebraic equations the Newton-Rhapson method is used. This method iteratively produces an increasingly accurate approximation of the solution. It is chosen as it is a robust method with a quadratic convergence rate, meaning that error decreases quadratically and thus decreasing computation time.
Newton's method makes use of linearization of the non-linear system of equations to come to a

linear set of equations that can compute the iterative correction. For the discretized system of Equation 3.5 the linear model is of the form,

$$\begin{aligned} \boldsymbol{K_1}(z^i)\delta\boldsymbol{p_c} &= -(\boldsymbol{r_1}(z^i) + \boldsymbol{q}) \\ \boldsymbol{K_2}(z^i)\delta\boldsymbol{S_f} &= -\boldsymbol{r_2}(z^i). \end{aligned} \tag{3.6}$$

In this equation K denotes the system Jacobian matrix and $\delta\boldsymbol{p_c}$ and $\delta\boldsymbol{S_f}$ refer to the iterative corrections for the capillary pressure and fiber saturation respectively. The iterative corrections are not depended on each other, because substitution of the value for the next increment is done with two separate functions which are not combined. Adding the iterative correction to the current iterative value gives the value for the next iteration,

$$\begin{aligned} \boldsymbol{p_c}(z^{i+1}) &= \boldsymbol{p_c}(z^i) + \delta\boldsymbol{p_c} \\ \boldsymbol{S_f}(z^{i+1}) &= \boldsymbol{S_f}(z^i) + \delta\boldsymbol{S_f}. \end{aligned} \tag{3.7}$$

Newton's method iterates until a certain convergence criteria is met. In this work the criteria is set on the residual. So the algorithm terminates when the residual is below a specified tolerance. The last iterative values in combination with the shape functions then give the numerical solution for the current increment.
To solve the non-linear system of equations with Newton's method, the two unknown system Jacobian matrices need to be determined. This can be done by substituting the value for the next increment into the equations for pore saturation, permeability and exchange term,

$$\begin{aligned} S_p(p_c^h + \delta p_c^h) &= S_p(p_c^h) + \frac{dS_p}{dp_c}\delta p_c^h \\ K_p(p_c^h + \delta p_c^h) &= K_p(p_c^h) + \frac{dK_p}{dp_c}\delta p_c^h \\ \Gamma(p_c^h + \delta p_c^h, S_f^h) &= \Gamma(p_c^h, S_f^h) + \frac{\delta\Gamma}{\delta p_c}\delta p_c^h \\ \Gamma(p_c^h, S_f^h + \delta S_f^h) &= \Gamma(p_c^h, S_f^h) + \frac{\delta\Gamma}{\delta S_f}\delta S_f^h. \end{aligned} \tag{3.8}$$

Substituting these expressions in the discretized system, Equation 3.5, gives a linear system of equations,

$$\int_{-\frac{H}{2}}^{\frac{H}{2}} \Big[\boldsymbol{N}\phi_p\frac{dS_p}{dp_c}\boldsymbol{N}^T - \frac{d\boldsymbol{N}}{dz}\Delta t\Big(\frac{K_p(p_c^h)}{\eta}\frac{d\boldsymbol{N}^T}{dz} + \frac{1}{\eta}\frac{dK_p}{dp_c}\frac{dp_c^h}{dz}\boldsymbol{N}^T\Big) + \boldsymbol{N}\Delta t\frac{\delta\Gamma}{\delta p_c}\boldsymbol{N}^T\Big]dz\delta\boldsymbol{p_c} = -(\boldsymbol{r_1} + \boldsymbol{q}) \tag{3.9a}$$

$$\int_{-\frac{H}{2}}^{\frac{H}{2}} \boldsymbol{N}\Big[\phi_f(1-\phi_p) - \Delta t\frac{\delta\Gamma}{\delta S_f}\Big]dz\delta\boldsymbol{S_f} = -\boldsymbol{r_2}. \tag{3.9b}$$

From this it becomes clear that the Jacobian matrices are given by,

$$\boldsymbol{K_1} = \int_{-\frac{H}{2}}^{\frac{H}{2}} \Big[\boldsymbol{N}\Big(\phi_p\frac{dS_p}{dp_c} + \Delta t\frac{\delta\Gamma}{\delta p_c}\Big)\boldsymbol{N}^T - \frac{d\boldsymbol{N}}{dz}\Delta t\Big(\frac{K_p(p_c^h)}{\eta}\frac{d\boldsymbol{N}^T}{dz} + \frac{1}{\eta}\frac{dK_p}{dp_c}\frac{dp_c^h}{dz}\boldsymbol{N}^T\Big)\Big]dz \tag{3.10a}$$

$$\boldsymbol{K_2} = \int_{-\frac{H}{2}}^{\frac{H}{2}} \boldsymbol{N}\Big[\phi_f(1-\phi_p) - \Delta t\frac{\delta\Gamma}{\delta S_f}\Big]dz. \tag{3.10b}$$

3.4 Application of boundary conditions

Within the numerical framework, essential and natural boundary conditions can be applied. To achieve this, the assembled system of equations must be partitioned as follows:

$$\begin{vmatrix} \boldsymbol{K_{1,uu}}^i & \boldsymbol{K_{1,uf}}^i \\ \boldsymbol{K_{1,fu}}^i & \boldsymbol{K_{1,ff}}^i \end{vmatrix} \begin{vmatrix} \boldsymbol{\delta p_{c,u}} \\ \boldsymbol{\delta p_{c,f}} \end{vmatrix} = - \begin{vmatrix} \boldsymbol{r_{1,u}}^i \\ \boldsymbol{r_{1,f}}^i \end{vmatrix} - \begin{vmatrix} \boldsymbol{q_u}^i \\ \boldsymbol{q_f}^i \end{vmatrix} \tag{3.11}$$

where the subscript u refers to nodes where the capillary pressures are prescribed, while the subscript f refers to the remaining nodes.
Considering an essential boundary condition, the capillary pressures in the nodes are known. Consequently, there is only one iterative correction required which sets the value in this node to the corresponding prescribed capillary pressure. Therefore, the value of $\delta p_{c,u}$ at the first iteration is set to the prescribed boundary value $\boldsymbol{p_c^*}$ and equals zero at the subsequent iterations

$$\boldsymbol{\delta p_{c,u}} = \begin{cases} \boldsymbol{p_c^*}, & \text{for } i = 1 \\ \boldsymbol{0}, & \text{for } i > 1. \end{cases} \tag{3.12}$$

The unknown iterative corrections $\boldsymbol{\delta p_{c,f}}$ can then be calculated by solving the following linear system of equations,

$$\boldsymbol{K_{1,ff}}^i \boldsymbol{\delta p_{c,f}} = -\boldsymbol{r_{1,f}}^i - \boldsymbol{q_f}^i - \boldsymbol{K_{1,fu}}^i \boldsymbol{\delta p_{c,u}}. \tag{3.13}$$

When a natural boundary condition is considered, the value of $\boldsymbol{q_u}^i$ is prescribed. Substituting this value for $\boldsymbol{q_u}^i$ in Equation 3.11 results in a linear system of equations the can be solve for $\delta \boldsymbol{p_c}$.

3.5 Model structure

The numerical model is structures into multiple modules to enhance the overall organization. This structure is visually depicted in Figure 3.1. It consist of a "main" module where simulation settings can be configured. These settings include inputs such as paper and liquid type, spatial and time dimensions, and Finite Element settings such as element size, iteration tolerance, and maximum iteration count. Subsequently, these settings are passed down to the "Parameters" module. This module adjusts parameters based on the specified inputs. This module is followed by the "Initialize" module, which handles spatial and time discretization, initializes the solution matrices, and sets the initial guess for the first Newton-Rhapson iteration. This initial guess is set to be the minimum capillary pressure of the medium plus an offset value,

$$p_{c,guess}(z) = p_{c,min} + p_{c,offset}. \tag{3.14}$$

In this work an offset value of $p_{c,offset} = 10^5$ Pa is utilized, as it yielded the most robust convergence outcomes. Once all values are initialized, the model progresses to the "Coating transport" module. This module focuses solely on the liquid transport through the coating. Here, the paper is not yet taken into account, as the liquid first needs to reach the interface between coating and paper. When the capillary pressure at the interface drops below the maximum capillary pressure of the paper, the model continues to the next module. This next module is called the "Coating-paper transport" module. In this module, as the name suggests, both the coating and paper are considered. The model stays within this module until the simulation time exceeds the user-specified end time. Subsequently, the model proceeds to the final "Plot" module, where the simulation data is post-processed and visualized on the screen.

Figure 3.1 also provides an overview of the "Coating transport" and "Coating-paper transport" modules. These modules are very similar, but have a few minor distinctions. One difference lies in the calculation of the iterative corrections. The "Coating transport" module only considers the capillary pressure iterative correction, while the "Coating-paper transport" module incorporates both the capillary pressure and fiber saturation iterative corrections. This is because it is assumed that bulk material of the coating solely facilitates liquid movement through its pores, without

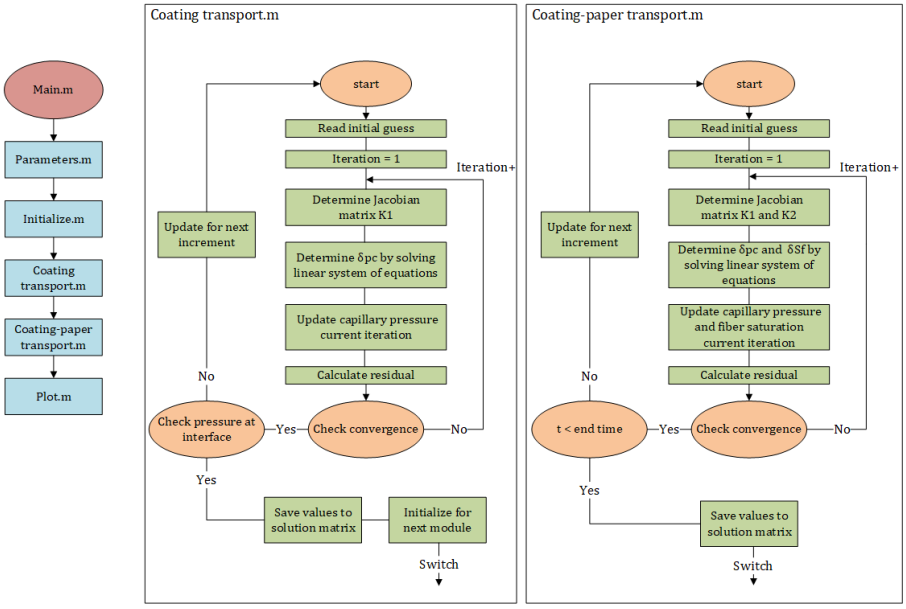

Figure 3.1: Visual depiction of liquid transport model structure.

absorbing any of the liquid. Hence, when only considering the coating the inclusion of the fiber saturation iterative correction becomes unnecessary due to the absence of interaction with the bulk material. Additionally, the "Coating transport" module features an initialization step before it proceeds to the next module, unlike the "Coating-paper transport" module, which does not have this initialization step. Within this initialization step, a new mesh which also includes the paper is generated and the initial guess is set for the next Newton-Rhapson iteration.

The update for the next increment has the same functionality for both modules. It involves resetting the residuals to zero, increasing the simulation time by the user-specified time step Δt, setting the initial guess for the Newton-Rhapson iteration, and calculating the total liquid volume in the sheet. This is done by determining the incremental change in liquid volume ΔV_l from the inflow at the boundaries,

$$\Delta V_l = A\boldsymbol{q_u}\Delta t \tag{3.15}$$

This incremental change is cumulatively added each increment to the total liquid volume in the pores at each increment. Initially, this volume starts at zero for a fully dry sheet. Through this approach, the model effectively monitors the amount of liquid in the sheet over time.

3.6 Mechanical model

From the resulting fiber saturation of the liquid transport model, the moisture content in the sheet is derived. This moisture content is then utilized to determine the elastic modulus and hygroexpansive strain in each node, iterated over all time steps. For each time step, Equation 2.32 is used to determine the average strain and curvature. The integrals in this equation are solved numerically using the trapezoidal integration method. This method approximates the region under the curve of an arbitrary function $f(z)$ by dividing it into a finite number of trapezoids. The summation of the areas of these trapezoids is the approximation to the integral,

$$\int_a^b f(z)dz \approx \sum_{i=1}^{N_{elements}} \frac{f(z_{i+1}) + f(z_i)}{2}\Delta z_i. \tag{3.16}$$

where $\Delta z_i = z_{i+1} - z_i$.

4 Experimental methods

At Canon Production Printing, two experimental setups are employed to study the effect of wetting (coated) paper sheets. In one of these test the paper is fully immersed in liquid, resulting in uniform wetting on both sides of the paper sheet. In this setup, only in-plane deformations are observed due to symmetric distribution through the sheet's thickness. This test offers valuable insights into the timescales of in-plane deformations, making it an ideal method for studying such behaviour. The second test only applies a limited amount of liquid to the top surface of an unconstrained paper sheet. In this case, the resulting through-thickness distribution of liquid is thus asymmetric. This asymmetric liquid distribution induces out-of-plane deformations in the unconstrained paper strip. The test setup is used to measure these out-of-plane deformations. This Chapter provides a concise overview of both experimental setups and their corresponding boundary conditions for modelling purposes. The results from these two test setups are presented in section 6 to validate the model.

4.1 Immersion test setup

The immersion test is used to measure the hygroexpansive strain of a paper sample in one-dimension. The sample is attached to a fixed and a movable clamp via magnets as depicted in Figure 4.1. The samples are cut at approximately 17 x 80 mm, where the length direction is orientated in the cross-machine direction [4]. To ensure that the sample is straightened, a small pre-tension of 0.05 N is applied at the movable clamp. The change in length of the sample over time is recorded by using a laser displacement sensor that is located at the fixed sample holder and aimed at the movable sample holder. The measured displacement divided by the initial length of the sample gives the hygroexpansive strain of the paper strip in the cross-machine direction. The liquid is applied by manually lifting a container filled with the liquid to fully immerse the sample.

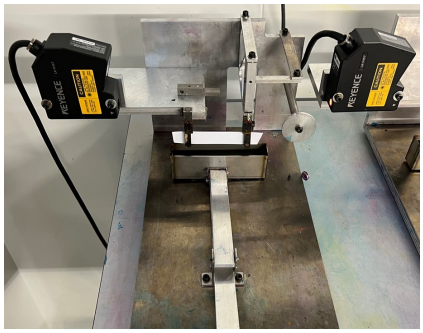

(a) Experimental setup.

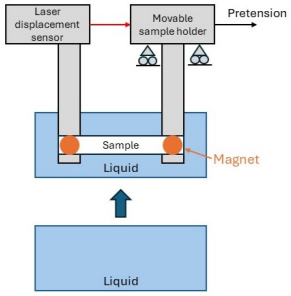

(b) Schematic overview.

Figure 4.1: Immersion test setup.

When the sample is fully immersed in the liquid, both surface of the sheet remain constantly wetted. The sample is thus subjected to symmetric boundary conditions. In the modelling context, it is then possible to apply a symmetry condition. In this case, only half the thickness of the paper sheet is considered, which helps in saving computation time. The outer surface of the sheet experiences a fully saturated condition, while the half-plane is subjected to a no-flow condition. Thus, the boundary conditions for the immersion test are as follows:

$$\frac{\partial p_c}{\partial z}(0,t) = 0 \tag{4.1a}$$

$$p_c(\frac{H}{2},t) = 0. \tag{4.1b}$$

The result obtained from the liquid transport model provides the fiber saturation through half of the sheet's thickness. This result is mirrored at the half-plane of the sheet to obtain the fiber

saturation throughout the entire thickness. Subsequently, this result is utilized by the mechanical model to determine the sheet's deformation.

4.2 Curl test setup

The curvature test setup prints 8.7 ml/m^2 of liquid onto a paper sample using a scanning printhead. The paper sample is attached to a support table with double sided sticky tape. A laser displacement sensor measures the out-of-plane deformation w of the paper sheet at a certain distance L from the support table, as shown in Figure 4.2. It is assumed that the through-thickness liquid distribution during this test is homogeneous along the length direction of the sample. Under this assumption, the downward curl of the sample, at a certain moment in time, is given by a constant curvature κ. This curvature can be calculated using straightforward trigonometry,

$$\kappa = -\frac{1}{R} = -\frac{2w}{L^2 + w^2}. \tag{4.2}$$

A minus sign is included here because downward curvature is regarded as negative in this study.

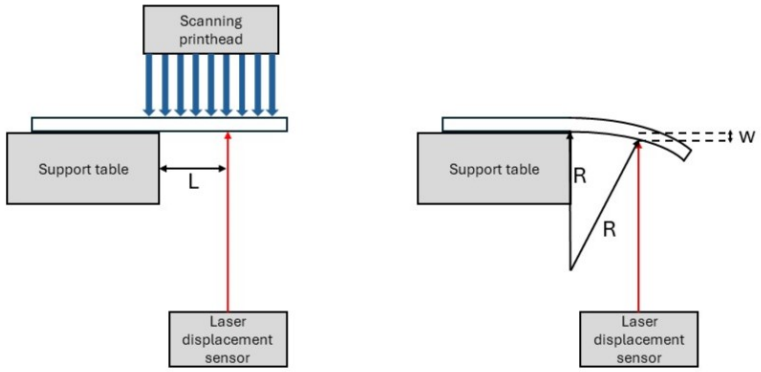

Figure 4.2: Curl test setup.

In the modelling context, the top surface of the sheet is in contact with the liquid until all the liquid is absorb by the sheet. So, as long as the liquid volume inside the paper sheet is lower than the applied volume of liquid, the boundary condition at the surface equals full pore saturation. However, once the liquid volume in the paper exceeds the applied amount, the boundary condition is switched to a no-flow condition, as no water flows into the paper sheet anymore. Conversely, at the bottom surface of the sheet, there is no liquid intake, so there is a no-flow condition at each instant in time. Hence, the boundary conditions are as follows:

$$\frac{\partial p_c}{\partial z}(0,t) = 0 \tag{4.3a}$$

$$p_c(H,t) = 0 \qquad \text{if } \frac{V_l}{A} < \frac{V_{intake}}{A} \tag{4.3b}$$

$$\frac{\partial p_c}{\partial z}(H,t) = 0 \qquad \text{if } \frac{V_l}{A} \geq \frac{V_{intake}}{A}. \tag{4.3c}$$

5 Model parameters

5.1 Medium properties

In this work two unsized paper types are considered: MondiCF and MondiNF. The parameters employed in the liquid transport model for these two types of paper are listed in Table 5.1. The parameters r_{min} and r_{max} were determined in the work of Dave et al. [4] by fitting the linear model to measured MIP data provided by Canon Production Printing. The porosity is also obtained from this test. The storage capacity of the fibers is deduced from the total expansion of the paper sheet in the immersion test, assuming that the fibers have the same hygroexpansive coefficient. The MondiNF paper type showed a greater expansion, leading to the assumption that the fibers in the MondiNF paper type have a higher liquid storage capacity.
For the coating, a single baseline type is considered. The parameters for this layer are taken from literature. The parameters r_{min} and r_{max} are estimated as the upper and lower limits of the pore sizes with the highest probability. The parameters describing the coating are later varied to investigate their influence on the liquid imbibition through the coating layer.

The parameters related to the fiber diffusion are also detailed in Table 5.1. Although the fiber storage capacity differs between the paper types, it is assumed that both paper types share identical fiber diffusivity and fiber thickness. Additionally, it is assumed that the fibers are entirely dry at the beginning of the simulation, meaning that there is no initial liquid content present in the fibers.

Table 5.1: Parameters paper types and coating.

	H $[\mu m]$	r_{min} $[\mu m]$	r_{max} $[\mu m]$	ϕ_p [-]	ϕ_f [-]	θ [°]	d $[\mu m]$	D $[m^2/s]$
MondiCF	89.4^d	0.05^a	2.05^a	0.4518^a	0.164	65^b	5^a	$0.4 \cdot 10^{-11}$
MondiNF	109^d	0.5^a	2.5^a	0.4312^a	0.175	65^b	5^a	$0.4 \cdot 10^{-11}$
Coating	15^d	0.01^c	0.1^c	0.34^c	-	45^c	-	-

Note: Data are from Dave et al. $[4]^a$, Muijtjens $[13]^b$, Yin et al. $[21]^c$ and measurement data provided by Canon Production Printing^d.

A visual representation of the three media is presented in Figure 5.1. Here the retention and permeability curves are given. The MondiCF paper type shows a small overlap in capillary pressure with the coating, as the maximum capillary pressure of MondiCF is slightly higher then the minimum capillary pressure of the coating. The MondiNF does not show this overlap in capillary pressures with the coating. Additionally, the coating shows the highest resistance against flow as it has the lowest permeability. This lower permeability is a result of the much smaller pores in the coating compared to the other media. The MondiNF paper shows the least resistance against flow, as this medium possesses the largest pores with respect to the other the two media.

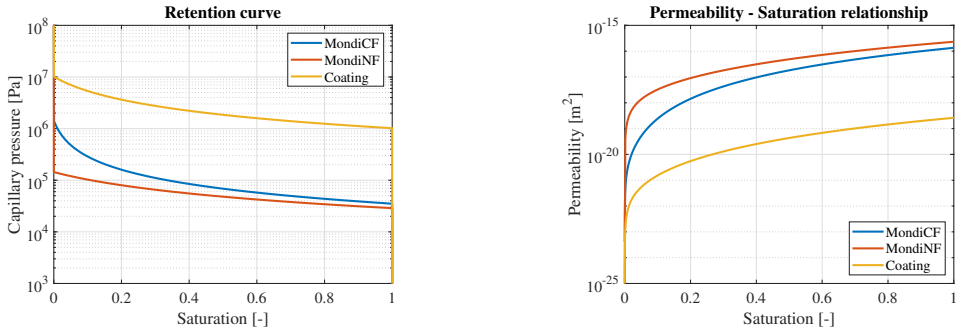

(a) Retention curve.

(b) Permeability function.

Figure 5.1: Visual representation considered media.

Finally the mechanical properties of the media are listed in Table 5.2. It is assumed that both paper types share the same mechanical properties. For the coating, the only relevant parameter is the elastic modulus. Under the assumption that that the bulk material of the coating does not absorb any liquid, it is expected that the elastic modulus does not decrease nor that the coating expands after wetting. Although the specific elastic modulus of the coating is unknown, it is estimated to be in the order of magnitude of $10 - 100MPa$ [1]. In this work, it is assumed that the elastic modulus of the coating is one-hundredth of that of a dry paper sheet, aligning with the order of magnitude of $10MPa$.

Table 5.2: Mechanical properties.

	E_{CD} $[MPa]$	χ_E [-]	β_{CD} [-]
Paper	$2.2 \cdot 10^3$ [a]	0.16[a]	0.25[a]
Coating	22	-	0

Note: Data are from van der Sman [18][a].

5.2 Liquid properties

The immersion test results for (coated) papers are based on tests conducted using demi water. One of the liquids used as input for the model is thus demiwater. In the parameter study, the effects of four other liquids are investigated. These liquids correspond to the ones utilized by Dave in his research. The mixtures consist of water, glycerol and hexanedial, which influences the viscosity and surface tension. The selected mixtures are chosen such that they represent the corners of the range of interest for viscosity and surface tension. This is visually depicted in Figure 5.2. The compositions of liquids, together with their respective viscosity and surface tension are summarised in Table 5.3.

Table 5.3: Liquid composition and properties.

Model liquid	Glycerole [m%]	Hexanediol [m%]	Water [m%]	Dye [m%]	Dynamic viscosity [mPas]	Surface tension [mN/m]
DW	0	0	100	0	0.89	72
1	48	10	41.9	0.1	7.2	27.5
2	25	10	64.9	0.1	3	26.8
3	57.5	0	42.4	0.1	7.9	68.0
4	25	0	74.9	0.1	1.7	70.5

Note: All data are from Dave (2020) [4].

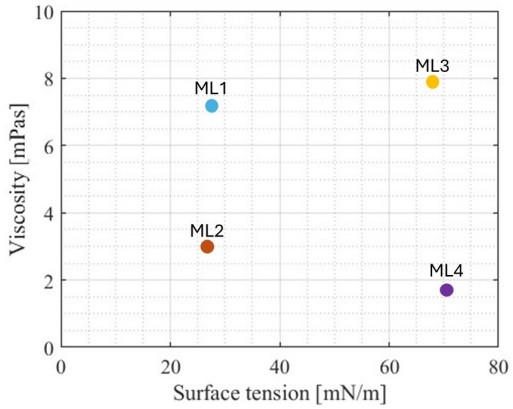

Figure 5.2: Surface tension and dynamic viscosity for liquids used in model.

6 Results

The results from the model shed light on the through-thickness moisture profiles of the pores and fibres, alongside the resulting deformation behaviour of the paper sheet over time. In this Chapter, these results are presented for two scenarios: a paper sheet fully immersed in liquid and a paper sheet wetted with a finite amount of liquid on its the top surface. The resulting time-scales regarding the deformations are validated with experimental data. First, a comparative analysis between the simulated and measured outcome from both the immersion and curl test are given. Subsequently, a parameter study is employed to analyze the influence of various inputs on the resulting time-scales regarding water imbibition in the coating layer.

6.1 Immersion test

Simulating the immersion test provides valuable information on the time-scales of liquid imbibition into the pores and fibers and subsequent deformation. Initially, the simulation is performed on an plain paper sheet to investigate the timescales in absence of a coating. This result serves as a reference in analyzing the effect of applying a coating. Subsequently, a coated paper sheet is simulated, and the results are compared with those obtained from the plain paper simulation. Finally, the resulting deformations of both the plain and coated paper sheets are compared with the measurements.

6.1.1 Liquid transport model results plain paper

Figure 6.1 shows the evolution of the through-thickness moisture distribution within the pores and fibers of a plain paper sheet immersed in demi water. The MondiCF paper type is used in this simulation and only half the paper thickness is considered. The pore saturation profile shows a front that moves through the thickness, eventually achieving full pore saturation after several tenths of milliseconds. Over time the sharp front transitions into a smoother profile. The smallest pores rapidly reach full saturation due to their responsiveness to high capillary pressures. Larger pores exhibit a slower uptake, because the magnitude of capillary action-driven flow is lower.

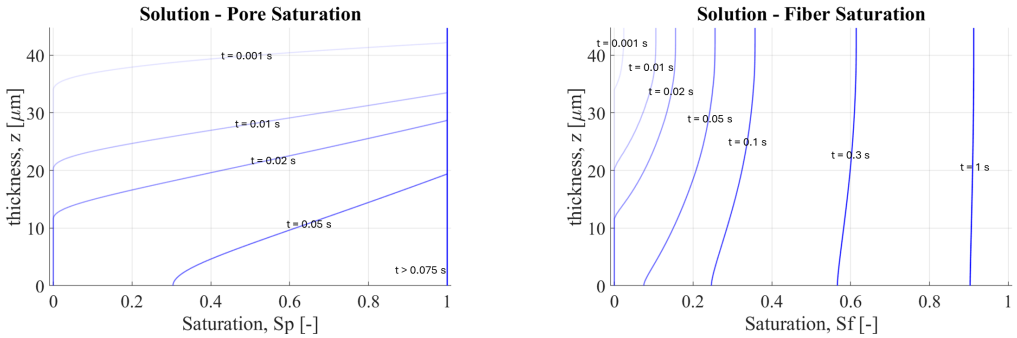

(a) Result pore saturation.

(b) Result fiber saturation.

Figure 6.1: Immersion test modelling results for plain paper MondiCF immersed in demi water.

Although the pores fully saturate within several tenths of milliseconds, the absorption of the liquid by the fibers occurs over a significantly longer period. Initially, there is a rapid increase to approximately a quarter of the fiber saturation, achieved around 0.1 seconds. Filling the remaining portion of the fiber takes, however, significantly longer. Full saturation of the fibers is only achieved after approximately two seconds. The significant difference in time scales between pore and fiber saturation is also clearly evident in the graphs showing the mean saturation over time, as depicted in Figure 6.2a. Liquid uptake by the fibers takes approximately 20 times longer than fully wetting the pores.

What is further evident from the results of the fiber saturation is that initially, as the liquid moves with a sharp front through the pores, only the outer regions of the sheet become saturated. This leads to an early increase of the fiber saturation towards the outer edges compared to the inner regions of the paper sheet. However, as time progresses, the fiber saturation profile gradually becomes more uniform through the thickness. During the fiber diffusion process, there is a rapid initial increase in fiber saturation. However, as the fiber saturation itself increases, the rate at which liquid enters the fibers decreases. Consequently, the fiber saturation in the inner regions catches up with that of the fibers in the outer regions.

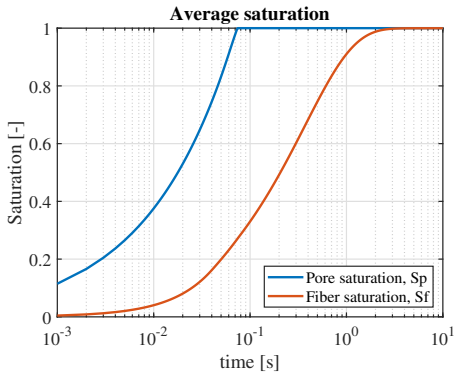

(a) Result average saturation.

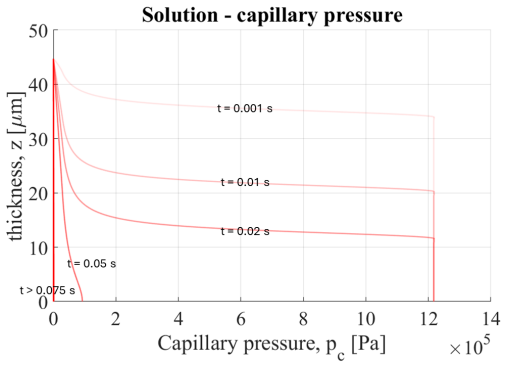

(b) Result capillary pressure pores.

Figure 6.2: Results average saturation and capillary pressure through the thickness in the pores.

Figure 6.2b shows the resulting capillary pressure profiles over time. These profiles exhibit a positive gradient, when viewed from the top surface of the sheet, through the saturated parts. This positive gradient in capillary pressure corresponds to a negative gradient in the total pressure, as can be derived from Equation 2.38. This pressure gradient is the driving factor behind the flow in the pores of the sheet. In the unsaturated regions, the gradient equals zero since there is no flow at that particular moment in time. Across the fully saturated regions, a linear pressure gradient can be observed. This indicates a constant flow throughout the thickness of this fully saturated region.

6.1.2 Liquid transport model results coated paper

The same MondiCF paper type is used to simulate a coated paper sheet. A coating with a thickness of $15\mu m$ is applied, while the paper thickness remains unchanged. This results in a total thickness of $119.4\mu m$, considering that the coating is applied on both sides of the paper. At Canon Production Printing, the overall thickness of coated papers was measured and revealed to be around 70-80 μm. This is considerably smaller then the thickness considered here. However, the specific paper type in these coated papers is unknown. Hence, it is plausible that the base layer thickness of the paper differs. The lower thickness also implies compression of the paper which can potentially alter the pore size distribution, leading to an increase in the number of smaller pores. Given the uncertainty regarding the effects of applying a coating on the parameters, it is assumed here that the base layer thickness and pore size distribution remain unchanged. The resulting through-thickness moisture distribution within the pores and fibers from the simulation is depicted in Figure 6.3, whereas the mean saturation and capillary pressure through the thickness are shown in Figure 6.4.

From the results it is evident that the coating almost fully saturates before any liquid goes into the paper. This is because the pores in the coating are much smaller and therefore favoured to fill first, due to their higher capillary pressures. The liquid will only start to move into the paper when the pores being filled in the coating match in size with the smallest pores in the paper, as shown in Figure 6.4b. In this graph, the black dashed line represents the maximum capillary pressure

of the paper, found in the smallest pores of the paper. When the capillary pressure inside the coating reaches this pressure, the gradient of capillary pressure within the paper start to change, initiating the flow of liquid into the paper. This happens when only the final, larger pores in the coating remain to be filled. Within the paper the liquid favors to move to the smaller pores deeper in the sheet at the cost of the larger pores near the top. This phenomenon arises from the limited supply in liquid via the coating and the higher capillary pressures of the smaller pores, which suck the water down towards the middle of the sheet.

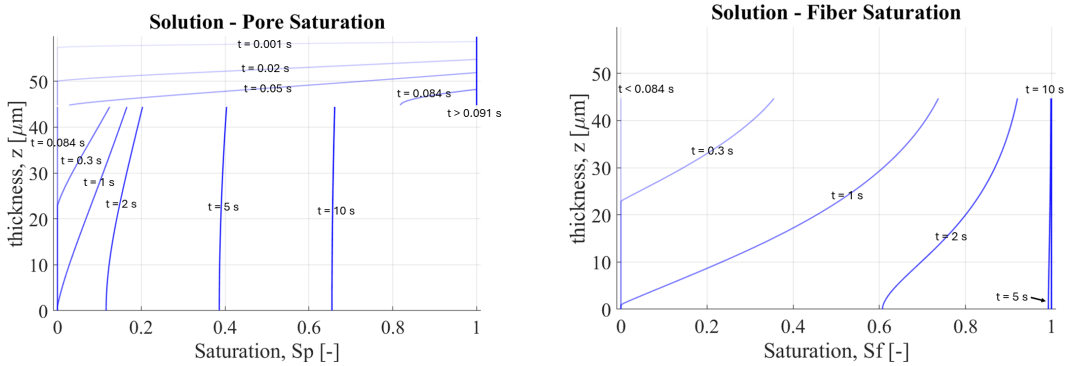

(a) Result pore saturation.

(b) Result fiber saturation.

Figure 6.3: Immersion test modelling results for coated paper MondiCF immersed in demi water.

Another interesting observation in the results of the immersed coated paper is the difference in total pore and fiber saturation. Figure 6.3a and Figure 6.4a indicates that the pores require a longer duration to achieve full saturation compared to the fibers. One plausible explanation for this phenomenon is that the liquid arriving in the pores goes straight into the fibers. As a result, the pores remain unfilled because the liquid supply via the coating is comparable to the exchange between pores and fibers.

When comparing the pore saturation profiles in the coated and plain paper sheets, as shown in Figure 6.1a and Figure 6.3a, one observes that the liquid progresses with a similar sharp front through the coating. Consequently, the onset of saturation in the paper pores exhibits a slight delay, approximately 0.084 s. Moreover, the rate of pore saturation is notably lower compared to a fully immersed plain paper. This is mostly due to the significantly lower permeability of the coated layer, as can be seen in Figure 5.1b. The liquid must first penetrate through a high resistance barrier before it can access the pores of the paper.

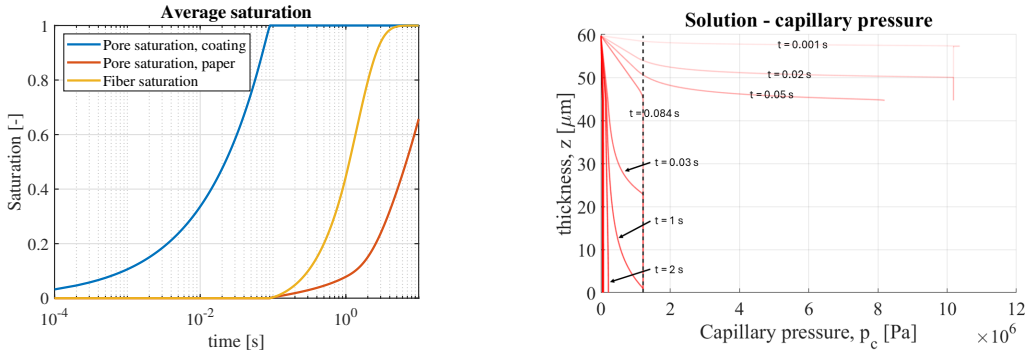

(a) Result average saturation.

(b) Result capillary pressure pores.

Figure 6.4: Results average saturation and capillary pressure through the thickness in the pores for a coated MondiCf paper sheet.

Due to the delayed onset of pore saturation, the fibers similarly experience a delay in wetting initiation. Since it takes considerably more time for the fluid to reach the inner regions of the paper, the onset of fiber saturation is significantly decreased here. This results in a substantial difference in fiber saturation through the thickness. Eventually, as the pores in the inner regions of the sheet begin to fill and the fibers increase in saturation, this difference in saturation through the thickness diminishes.

6.1.3 Resulting strain time evolution

The results from the water transport model serve as input for the mechanical model. The simulated fiber saturation through the thickness is used to determine the hygroexpansive strain. Figure 6.5 shows the average strain versus time plot derived from the mechanical model for both paper types, with and without coating. Additionally, experimental results are included for comparison. However, it is worth noting that the base layer type in the coated papers differs from that used in the model. Consequently, comparing results between the model and experiment for coated papers is only valid on a qualitative basis.

Comparison of the results for plain paper between the model and experiment reveals that the model tends to overpredict the initial increase in average strain. This discrepancy suggests that either the timescale of liquid imbibition in the pores is underestimated, or the initial rate at which the fibers take up water is too large in the model. Another factor which might contribute to this discrepancy could be the calibration in the measurements. It takes a few milliseconds to fully submerge the sample by lifting the container with liquid. Calibrating the onset of average strain to the precise time in the measurements might introduce a small error. Since the results are compared on a logarithmic time scale, even the slight difference of a few milliseconds can show a small discrepancy in the result.

Another difference between the model and measurements is observed when the paper reaches full saturation. In the experimental results, the average strain continues to increase over time, whereas in the model, the average strain becomes constant after approximately three seconds. This continued increase in average strain after full saturation has been investigated in the work of Muijtjens [13]. In his work, he concluded that this phenomenon is likely due to the effect of creep caused by the initial pre-tension applied to the sample. As the effect of creep is not accounted for in the mechanical model, this effect is not visible in the model results.

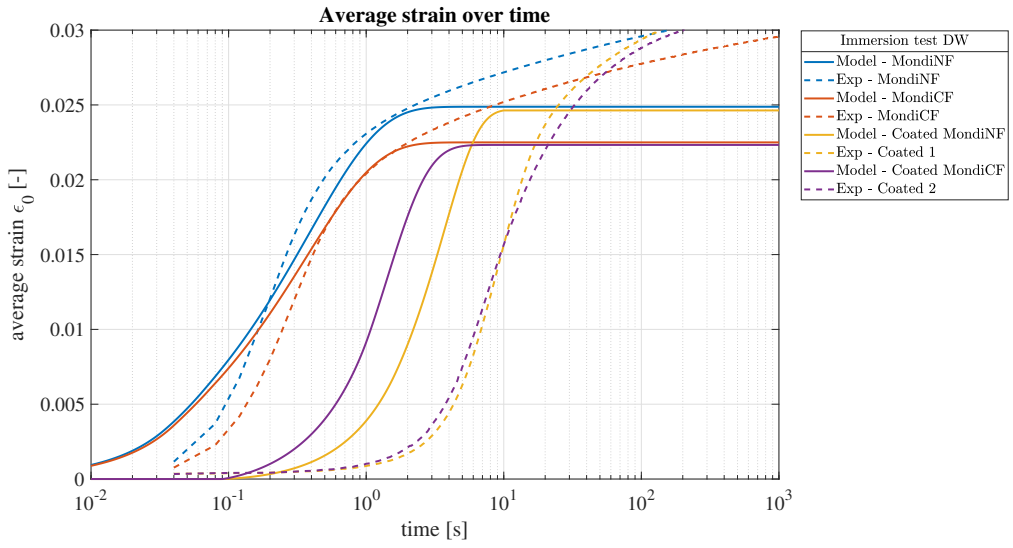

Figure 6.5: Results average strain over time from the mechanical model and measurements.

The model results for the coated paper sheets exhibit a slight delay in the onset of average strain, approximately 0.084 s. This delay is equivalent to the time required for the liquid to travel through the coating and reach the top surface of the paper, as can be seen in Figure 6.3a. One can observe that for the coated MondiNF paper type, the initiation of average strain occurs slightly later. This small difference arises because the minimal pore size in the MondiCF paper is larger than the maximum pore size of the coating. Consequently, the entire coating saturates before the paper pores commence saturation. The mondiCF paper features a lower maximum pore radius compared to the maximum pore size of the coating. Thus, the paper pores commence saturating before total coating saturation is achieved. The experimental results on coated paper sheets also reveal a delay in average strain initiation. However, this delay is slightly longer, indicating that the liquid travels at a slower pace through the coating than is predicted by the model. Additionally, the converged average strain value is marginally lower for the coated papers compared to the plain papers. This slight difference arises because the coating does not expand upon saturation, thereby adding some resistance to the overall expansion of the sheet. However, since the elastic modulus of the coating is several orders of magnitude lower than that of paper, the overall resistance is minimal.

6.2 Curl test

The curl test provides additional insights into the out-of-plane behaviour of a paper sheet when exposed to a liquid. Again, an initial simulation is performed on an plain paper sheet to investigate the timescales in the absence of a coating. However, the model liquid ML4 is used as the fluid in the simulation instead of demi water. This choice is made, because demi water cannot be used in the experimental setup, thus no data is available for this fluid. The model liquid ML4 is also used to simulate the liquid transport through the coated paper. Finally, the results obtained from the plain paper simulation are compared with the experimental data from the curl setup and the simulated data from the coated paper.

6.2.1 Liquid transport model results coated paper

Figure 6.6 shows the evolution of the through-thickness moisture distribution within the pores and fibers of a plain paper sheet subjected to a finite liquid droplet. The volume per squared meter of this droplet equals $8.7ml/m^2$. Within the simulation, the whole thickness H of the sheet is considered, as the problem is not symmetric. Until a time of approximately $0.02s$, a similar front to that observed in the immersion test is noted. Until this moment, the liquid moves from the surface of the sheet inside the pores. After this point, the saturation at the surface starts to decrease because all the liquid moved from the surface into the sheet. Consequently, the liquid in the pores starts to redistribute itself through the thickness while simultaneously flowing into neighbouring fibers. As a result of this transport into the fibers, the saturation in the pores gradually decreases over time, as can be seen in Figure 6.7a.

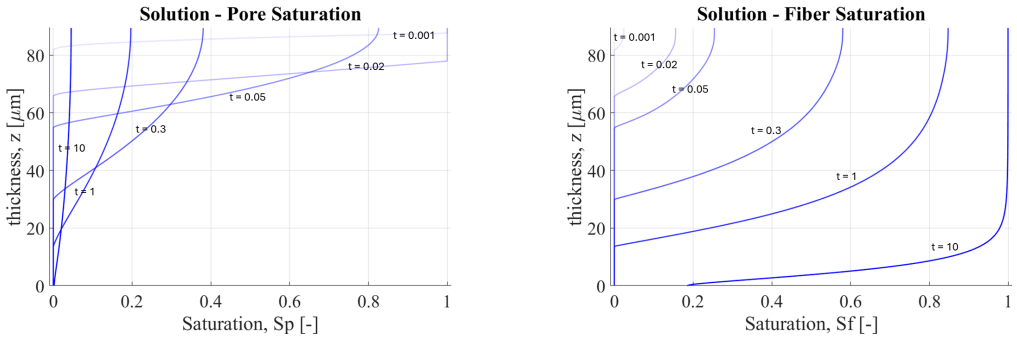

(a) Result pore saturation.

(b) Result fiber saturation.

Figure 6.6: Curl test modelling results for plain paper MondiCF immersed in model liquid ML4.

From the resulting evolution of the fiber saturation, as shown in Figure 6.6b, it is evident that the fibers saturate from top to bottom. Since only the top side of the sheet is saturated, the fibers in the upper regions initiate saturation earlier in time. It takes some time before the pores in the bottom regions fill, resulting in delayed initiation of fiber saturation in those regions. Consequently, this leads to a longer duration until full fiber saturation is achieved compared to the immersion test, as can be seen in Figure 6.2a and Figure 6.7a. In the immersion test, where both sides of the sheet are saturated, overall saturation occurs faster because the liquid effectively needs to travel less deep into the sheet. Additionally, the immersion test consist of an infinite amount of liquid, which accelerates the process since the saturation inside the pores does not decrease. Finally, model liquid ML4 has a higher viscosity than demi water. This higher viscosity hinders the flow of liquid ML4 through the porous medium, consequently increasing the pore and fiber saturation duration.

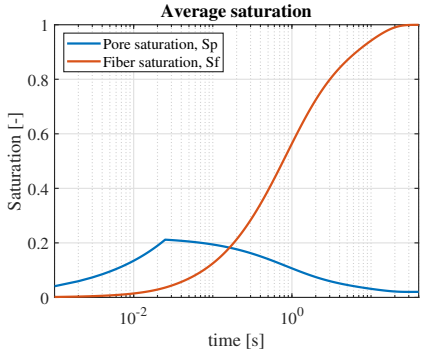

(a) Result average saturation.

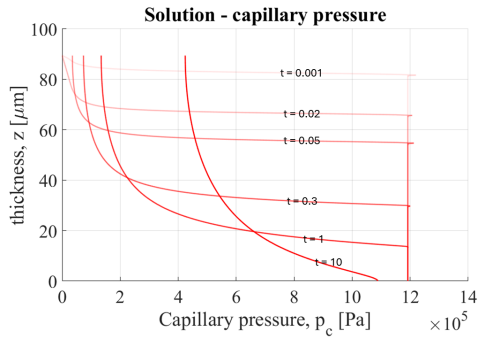

(b) Result capillary pressure pores.

Figure 6.7: Results average saturation and capillary pressure through the thickness in the pores.

The resulting capillary pressure profiles are shown in Figure 6.7b. Initially, the capillary pressure at the top surface equals zero, which is in accordance with the essential boundary condition. After approximately $0.02s$, the boundary condition transitions to a no-flow condition, indicating that all the liquid from the surface has entered the sheet. From this point onward, the capillary pressure at the top begins to increase because pores are being emptied. This process starts with the largest pores, which have the lowest capillary pressures. As time progresses, smaller pores start empty, leading to the gradual increase in capillary pressure.

6.2.2 Liquid transport model results coated paper

In the simulation involving coated paper, a coating with a thickness of $15\mu m$ is applied, while the paper thickness remains unchanged. The resulting evolution profiles of saturation are depicted in Figure 6.8. The results reveal a similar delay in onset of paper pore saturation as observed in the model results of the immersion test. This delay is again attributed to the smaller pores in the coating being filled first. Around approximately $0.0165s$, when the coating is almost fully saturated, the liquid starts to move into the paper. The overall pore saturation increases until the finite amount of liquid at the top surface has been absorbed by the sheet. Subsequently, the paper pore saturation begins to decline, while the coating pore saturation remains fully saturated, as shown in Figure 6.10a. The liquid favors to move from the larger paper pores toward the bottom of the sheet rather than from the smaller coating pores. As the capillary pressure rises, it first depletes the pores with the lowest capillary pressures, associated with the larger paper pores. The capillary pressure in the coating remains below the minimum capillary pressure of the coating, as indicated by the blue dashed line in Figure 6.10b, and thus the saturation remains at one. After the absorption of all liquid on the top surface by the sheet, the overall pore saturation shows a decrease. This result mirrors to findings from the plain paper simulation, and is a result of the liquid moving into the fibers.

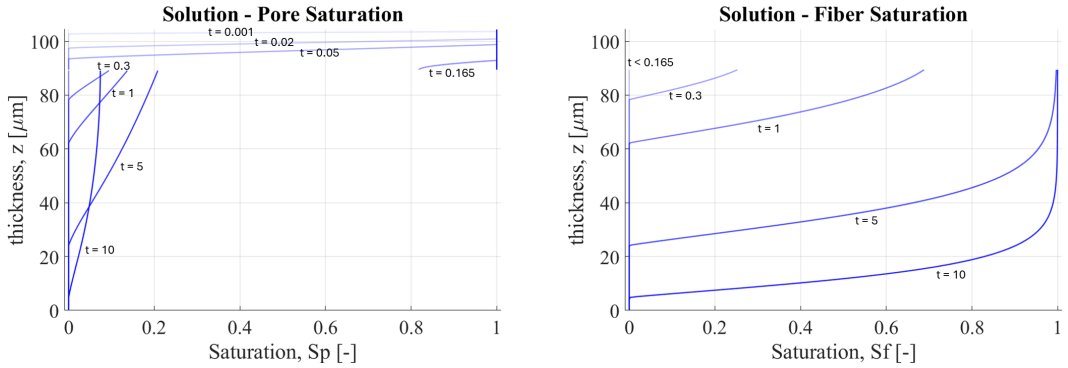

(a) Result pore saturation.

(b) Result fiber saturation.

Figure 6.8: Immersion test modelling results for coated paper MondiCF immersed in demi water.

Compared to the plain paper simulation, the maximum average paper pore saturation is notably lower. This lower saturation is because the coating also absorbs a portion of the total amount of liquid applied at the top surface. Consequently, less liquid volume infiltrates the paper pores before the liquid at the top surface is entirely absorbed by the sheet. Additionally, the flow within the paper pores is significantly reduced compared to the plain paper simulation. This decrease in flow is a results of the lower permeability of the coating that acts as a barrier. Consequently, the liquid tends to enter the fibers more rapidly than it progresses through the thickness within the pores. This leads to a steep increase in fiber saturation, as can be seen in Figure 6.8b.

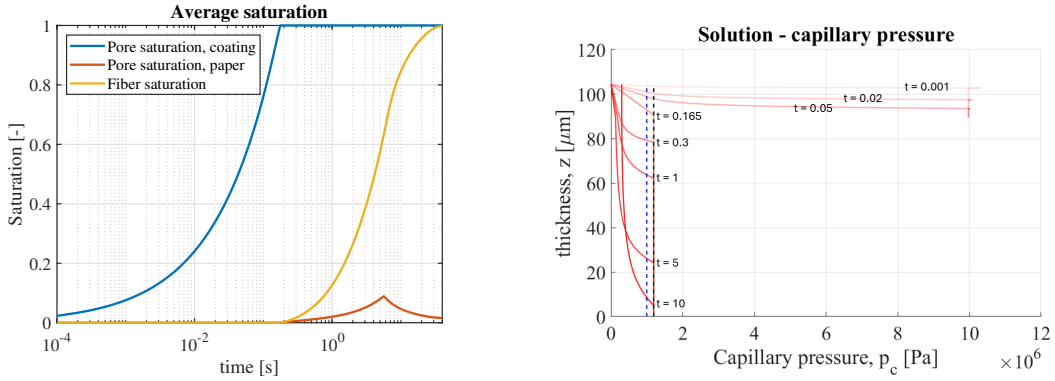

(a) Result average saturation.

(b) Result capillary pressure pores.

Figure 6.9: Results average saturation and capillary pressure through the thickness in the pores.

6.2.3 Resulting strain time evolution

The mechanical model, coupled with the results of the liquid transport simulation, is utilized to determine the curvature over time. In Figure 6.9a, the results from the model are illustrated for both plain and coated paper. Additionally, experimental data from test conducted on a plain MondiCF paper sheet are included. Since there is no available data for coated paper, the results from the coated paper simulation are compared with those from the plain paper simulation.

Comparison between the model and experiment reveals that the model tends to over predict the maximum curvature by approximately a factor of 1.7. This overestimation suggests that the predicted distribution in hygroexpansive strain through the thickness is too sharp. One factor that can likely influence this distribution is the fiber diffusion. As the fiber diffusion decreases, the liquid can flow more easily to the pores at the bottom of the sheet. Consequently, the onset

of fiber saturation at the bottom of the sheet starts earlier, resulting in a more gradual increase in fiber saturation. As the fiber saturation increases more gradually through the thickness, the maximum curvature of the sheet decreases. One factor that influences the rate of diffusion is the fiber diffusivity. It is possible that the fibers experience a different fiber diffusivity when in contact with model liquid ML4 compared to demi water.

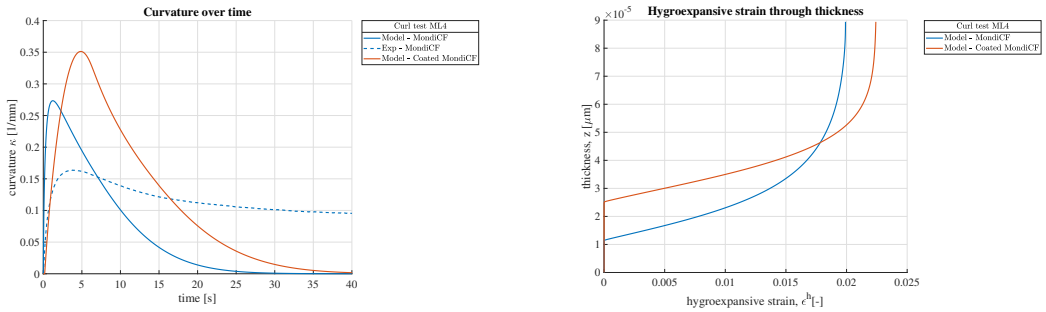

(a) Result curvature.

(b) Hygroexpansive strain.

Figure 6.10: Results curvature over time and hygroexpansive strain in the sheet at maximum curvature.

The experimental data also reveals a gradual decrease in curvature after reaching maximum curvature, which is considerably slower compared to the simulation results. The slower rate at which uniform saturation is reached is thus much lower then the model predicts, again indicating a potential overestimation in fiber diffusion. The presence of fillers and other additives in the paper likely influences the rate at which full saturation is reached [4]. Additionally, the absence of modelling the plastic strain in the simulation could contribute to the faster decrease in curvature observed in the model. In the pure elastic case, the internal stresses within the paper approach zero as the fibers become more uniformly saturated. Factors such as creep and plasticity could potentially be influencing the long term curvature behaviour.

When comparing the coated paper to the plain paper, it is evident that the coated paper reaches a higher maximum curvature. To examine the difference between the two media, the resulting hygroexpansive strain through the thickness is plotted at the time the sheet is at maximum curvature in Figure 6.10b. It can be observed that in plain paper, the distribution of fiber saturation is slightly more gradual compared to the coated paper. In the coated paper, the liquid has mostly entered the fibers in the top regions of the paper, resulting in a significant difference in hygroexpansive strain throughout the thickness. This larger hygroexpansive strain is attributed to the slower rate at which the liquid moves through the pores in the coated paper. According to the model, the reduction in liquid flow within the paper leads thus to larger curvature in the sheet. One might argue that the coating could potentially act as a resistance against the curvature. However, as already evident from the results of the immersion test, the resistance of this layer is not significant due to its low elastic modulus test.

6.3 Parameter study

The model is now subjected to several parameter variations to study the effect of these parameters on the penetration time and mechanical expansion. A sweep over the coating thickness, pore radii, porosity and contact angle is conducted to study the influence of the coating on the penetration time. Furthermore, the model is executed with the four different model liquids from Table 5.3 to investigate the effect of various fluids on the mechanical expansion time of the coated paper sheet.

6.3.1 Coating properties

Figure 6.11 shows the results from the sweep over the coating properties. The value on the y-axis corresponds to the time at which the paper pores initiate saturation, i.e. the time delay induced by the liquid penetrating through the coating. An increase in contact angle leads to a longer penetration time. For contact angles between 0 and 50 degrees a gradual increase is observed of approximately $0.03s$. However, particularly for relatively large contact angles, this increase is significantly greater. From a contact angle of 50 to 80 degrees an increase of approximately $0.22s$ is observed. This aligns with expectations, as higher contact angles introduce greater resistance to imbibition, and contact angles higher than 90 degrees even prevent imbibition altogether.

The coating thickness is varied between 5-15 μm, which are commonly utilized in coating applications [7]. From the parameter study it can be concluded that increasing the coating thickness leads to a nearly linear rise in penetration time. Increasing the coating thickness with $5\mu m$ leads to an approximate increase of $0.025s$. Here an increase from 10 to 15 μm, shows a slightly bigger increase than increasing from 5 to 10 μm, showing the the increase is not entirely linear. This increase in penetration time for thicker coatings aligns with expectations, considering that a thicker coating requires the liquid to travel a greater distance.

The porosity exhibits no visible effect on penetration time according to the model. Equation 2.4a and Equation 2.13 explains this behaviour. The last term in Equation 2.4a can be neglected when only considering the coating, because there is no exchange from the pores to the surrounding bulk material. By substituting the formulation for the permeability, Equation 2.13, into Equation 2.4a and considering a constant porosity through the thickness, the porosity can be isolated. From this, the porosity can be divided out of the equation, meaning that it has no influence on the results.

Finally, increasing pore size at constant porosity results in a decrease in penetration time. This decrease is particularly notable for very large pores where the decrease is considerable. It is also noteworthy that a substantial decrease in large pore radius leads to an exponential grow in penetration time.

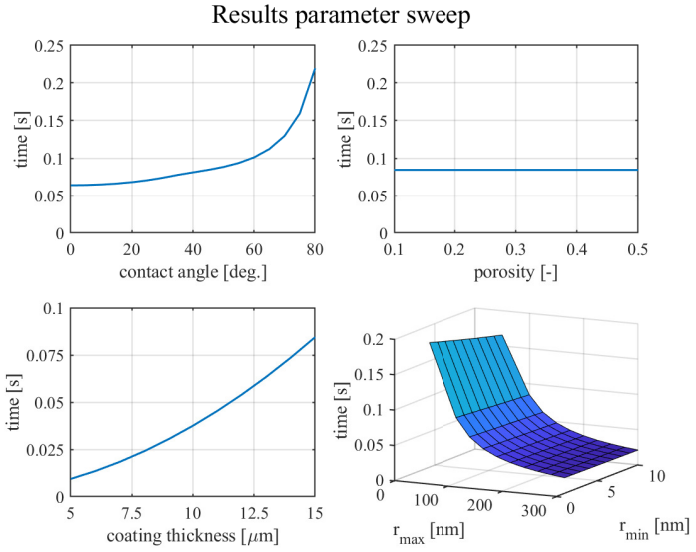

Figure 6.11: Results average strain over time from the mechanical model and measurements.

6.3.2 Liquid properties

Figure 6.12 presents the model and experimental results for the four different liquids. Upon examining the results, it becomes apparent that model liquid four exhibits the shortest expansion duration. This liquid also contains the highest water mass percentage compared to the other model liquids. Introducing Hexanediol or Glycerole into the mixture significantly prolongs the elongation period, as can be seen from the results of the other model liquids. Addition of Hexanediol reduces the surface tension of the mixture, thereby decreasing capillary pressures within the pores. This decrease leads to lower capillary action-driven flow, which in turn extends the saturation times. The addition of Glycerole increases the mixture's viscosity. Liquids with high viscosity experience greater resistance against flow compared to liquids with a low viscosity, leading to extended saturation times. Thus, by adding Hexanediol or Glycerole to the mixture, saturation times increase and the sheet's elongation time is prolonged.

The model yields similar elongation times for model liquids ML2 and ML3. However, according to the experimental data, ML2 exhibits elongation times much closer to ML4, while ML3 tends to shows similar elongation times to ML1. These measurements indicate that the viscosity has a significantly greater impact on the elongation times than the surface tension of the liquid. On possible explanation for this observation is the difficulty with which a highly viscous fluid wants to infiltrate the fibers. The fiber diffusivity term is based on demi water entering the fibers of the paper, which has a relatively low viscosity. ML2 and ML4 have a slightly higher viscosity with respect to demi water, however ML1 and ML3 how much higher viscosity's. This discrepancy in viscosity could potentially explain why ML2 and ML4, and ML1 and ML3, exhibit similar elongation times.

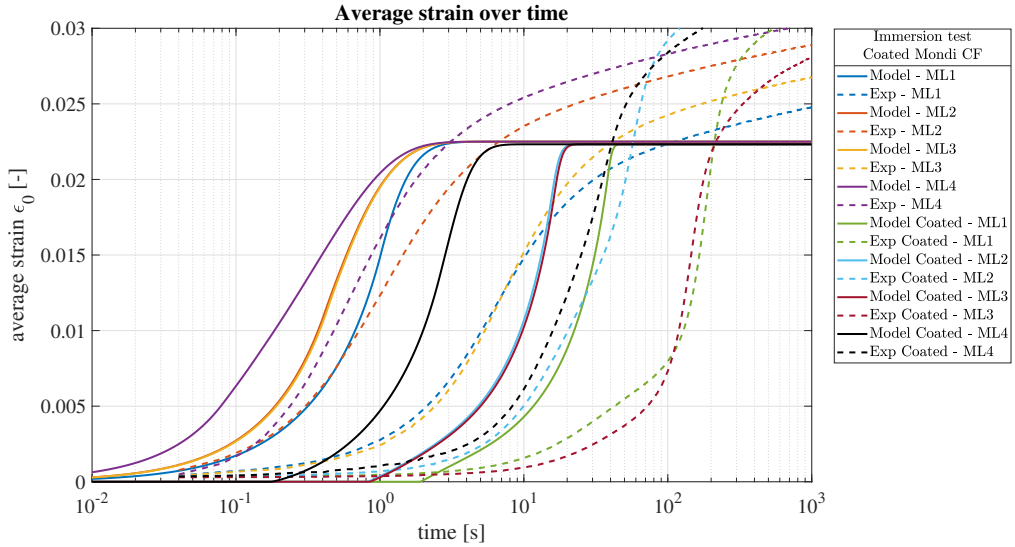

Figure 6.12: Results average strain over time from the mechanical for different liquid models.

7 Conclusion

The main goal of this study was to understand the physics behind the liquid transport in coated paper sheets and the subsequent mechanical deformations. To achieve this, a one-dimensional numerical framework is extended to also account for coated papers. This original framework simulates the capillary-driven flow through a porous-fibrous network and subsequent interaction with cellulose fibres. At its core, the model employs the classical Richards equation, which is widely used to describe flow through porous media. To this balance equation, liquid exchange between pores and fibers is added. The liquid transport from pores into the cellulose fibers is modeled using a one-dimensional diffusion equation. Relationships between saturation, capillary pressure and permeability are derived from measured pore size distribution of plain paper sheets. The transport model is coupled with a hygro-elastic mechanical model to describe fiber swelling and provide insights into sheet's hygro-expansion.

Validation of the model is conducted through an immersion test. This experiment measures the hygro-expansion of fully immersed (coated) paper sheets. A comparison between experimental data and model predictions revealed that the model is able to predict the overall deformation time scale for a plain paper immersed in demi water quite well. Only the initial strain showed a slight overestimation, although at these small time scales, there is also some uncertainty in the measurements. Moreover, the model is able to predict a delay in deformation onset in coated papers due to the time scales associated with liquid movement through the coating. It was also revealed that the coating significantly extends the time scales for liquid movement through the paper pores, primarily due to the lower permeability of the coating. Consequently, this leads to an extended duration for fibers to saturate, resulting in increased overall deformation times. Qualitatively, these timescales were also apparent in the measurement. However, a precise quantitative match between the model predictions and measurements was not achieved due to numerous uncertainties associated with the properties of coated papers.

Model predictions were also compared with measurement data from a curl test, which measures the sheet's curvature over time following the application of a finite amount of liquid on the top surface. Comparison between model predictions and measurement data for plain paper revealed an overestimation of the maximum curvature by approximately a factor of 1.7. Moreover, discrepancies were observed in the decrease of curvature after reaching this maximum curvature. The model predicted a rapid decrease to zero curvature, while data from measurements revealed a slow decrease that did not return to zero.
Comparison between model predictions for plain and coated paper showed that the coated paper experienced a larger maximum curvature. This was accompanied by a steeper hygroexpansive strain profile observed in the sheet at the time of maximum curvature. This steep profile arises from the slower movement of liquid through the thickness, primarily saturating the upper fibers in the sheet. According to the model, this reduction in liquid flow, attributed to the resistance of the coating, leads to larger curvatures.

The model was also subjected to a parameter study. Increases in contact angle, viscosity or coating thickness prolong the duration of liquid traveling through the coating before initiation of paper pore saturation, whereas an increase in pore size or surface tension showed a decrease in penetration times. The porosity did not show any notable changes in penetration times.
Furthermore, four model liquids were employed to investigate the effect of viscosity and surface tension. It was found that increasing either viscosity or surface tension resulted in an increase in deformation times. However, there were differences in magnitude between the results from measurement data and model predictions. The measurements showed that viscosity had a much greater impact on deformation times compared to surface tension, whereas he model predicted these effects to be roughly the same. The comparison between model predictions and measurements data might suggest that higher viscosity fluids may encounter more difficulties in entering the fibers.

Although the model exhibits some deviations in initial strain increase and long-term expansion behaviour, the influence of coating application is evident from the model predictions. A total understanding of the physics behind the liquid transport and subsequent mechanical deformations is thus not achieved. However, the model gives some understanding on the delay of mechanical deformations in coated paper sheets. This delay is primarily attributed to reduced pore sizes and lower permeability in the coating layer. Further research on topics like pore-fiber exchange, permeability function and elasto- and viscoplasticity could enhance accuracy and deepen understanding of the underlying physics.

8 Evaluation & Outlook

Throughout this study, certain assumptions have been made which influence the results of the model. This Chapter evaluates these assumptions and offer suggestions for future research to gain a deeper understanding of liquid penetration in coated paper sheets.

One aspect of the model that requires further investigation is the transport of liquid from pores into fibers. In this work, a one-dimensional diffusion model has been proposed to describe the transport from a single pore into its neighbouring fibers. The summation of these local fiber saturations yields the global fiber saturation at sheet level. For relatively quick pore saturation this describes the transport behaviour quite well. Only the initial rate of fiber saturation seems to be slightly overestimated by the model. In the context of a coated paper, pore saturation is drastically reduced. This reduction leads to substantial time delays in pore saturation initiation within larger pores. This delay in larger pores suggest that smaller pores may saturate a region larger than assumed by the local fiber diffusion equation. Consequently, the time for the fibers to saturate is likely prolonged. Utilizing a more sophisticated model capable of accounting for these large variations in pore saturation onset would provide deeper insights into the fiber saturation. Additionally, the effect of viscosity on fiber diffusion still remains uncertain. The model shows significant differences in the elongation times of the four model liquids with respect to the measurements. This could potentially be a results of decreased fiber saturation for higher viscosity fluids. Further research into this might give more insights in the response of (coated) paper sheets to various liquids.

Additional investigation is needed into the the permeability model within the water transport model. This study employs a simplistic permeability model derived from a porous block with cylinders of varying radii. However, this model tends to overestimate the permeability significantly, leading to the introduction of a scaling factor to account for this. Despite this correction, the utilized permeability model shows higher permeability at low saturation compared to the widely accepted van Genuchten model. Unfortunately, attempts to implement van Genuchtens permeability model resulted in convergence errors in the current numerical setup of the water transport model. Investigating these convergence issues further to enable the utilization of the van Genuchten model could yield additional insights into the penetration time through (coated) papers. Moreover, investigating more sophisticated permeability models could offer deeper understanding of the underlying processes governing liquid penetration. It is worth considering building upon the research conducted by van der Wijst [20] and Ploumen [15].

The current mechanical model is very simplistic: only elastic and hygro-expansive strain are considered. Yet, paper exhibits viscoelastic and viscoplastic behaviour. This behaviour is evident in the measurements, which reveal creep strain over prolonged periods. Integrating this behaviour in the model would offer greater understanding of the mechanical deformations over extended durations. This includes conducting creep measurements at various moisture contents to gather creep data for calibrating the model. Additionally, performing tensile tests on a coating sample could give more insight in the elastic modulus of the coating. Currently the coating's elastic modulus is assumed to be 100 times lower than the elastic modulus of paper. A more accurate determination of the coating's elastic modulus could give more insights into its resistance against global sheet deformation.

An interesting observation from the measurements, simplified in the model, concerns the paper thickness in the coated papers. Measurements revealed a total sheet thickness ranging from $70-80\mu m$, with a coating thickness of roughly $15\mu m$ on both sides. This suggests that the paper thickness is around $40-50\mu m$, which also implies that the pore size distribution might be affected due to compression of the paper. In the model, the base layer thickness with a plain paper pore size distribution is used for the paper layer. The reduced thickness in the measured coated papers might imply that the liquid penetration is faster than predicted by the model. However, smaller

pore sizes due to compression implies prolonged liquid penetration. These opposing effects due to thickness reduction and smaller pores counteract each other. However, the extent of each effect remains uncertain. Further investigation into the decrease in sheet thickness and possible alterations in pore size distribution could lead to deeper understanding of the liquid penetration in coated paper sheets.

Finally, the model is limited to predicting liquid transport solely through the thickness of the paper sheet. Hereby it is assumed that the in-plane liquid distribution is uniform, meaning that only uniform wetting of paper sheet's top surface can be analyzed. To investigate the effect of partial saturation of the top surface, such as when applying a droplet, the model needs to be extended to higher dimensions.

References

[1] P Alam et al. "The elastic modulus of paper coating in tension and compression". In: *TAPPI Coating and Graphics Arts Conference*. TAPPI Press, 2007.

[2] T. Alleborn and H. Raszillier. "Dynamics of films and droplets spreading on porous substrates". In: *Tappi Journal* 6 (2007), pp. 16–23.

[3] R.H. Brooks and Corey A.T. "Hydraulic properties of porous media". In: *Hydrology paper* 3 (1964).

[4] N. Dave et al. "Hydro-expansion of thin porous-fibrous sheets induced by through-thickness liquid penetration: pore transport, fibre mass exchange and moisture-induced deformations". in preperation.

[5] Hans-Jörg G. Diersch. *FEFLOW: Finite Element Modeling of Flow, Mass and Heat Transport in Porous and Fractured Media*. Springer Berlin, Heidelberg, 2013. DOI: 10.1007/978-3-642-38739-5.

[6] R.T. Fenner and J. N. Reddy. *Mechanics of Solids and Structures*. Boca Raton: Taylor & Francis Inc, 2012. DOI: doi:10.1201/b11931.

[7] P.A.C. Gane et al. "Fluid transport into porous coating structures: Some novel findings". In: *Tappi Journal* 83 (Jan. 2000), pp. 77–78.

[8] M. Th. van Genuchten. "A Closed-form Equation for Predicting the Hydraulic Conductivity of Unsaturated Soils". In: *Soil Science Society of America Journal* 44.5 (1980), pp. 892–898. DOI: 10.2136/sssaj1980.03615995004400050002x.

[9] G. Gottardi and M. Venutelli. "Richards: Computer program for the numerical simulation of one-dimensional infiltration into unsaturated soil". In: *Computers & Geosciences* 19.9 (1993), pp. 1239–1266. ISSN: 0098-3004. DOI: 10.1016/0098-3004(93)90028-4.

[10] Henk Huinink. *Fluids in Porous Media*. 2053-2571. Morgan & Claypool Publishers, 2016. DOI: 10.1088/978-1-6817-4297-7.

[11] B. A. G. Lomans. "Predicting paper sheet curvature and strain due to through-thickness moisture gradients". Technical University Eindhoven, 2016.

[12] Y. Mualem. "A new model for predicting the hydraulic conductivity of unsaturated porous media." In: *Water Resources Research* 12.3 (1976), pp. 512–522. DOI: 10.1029/WR012i003p00513.

[13] R. R. L. Muijtjens. "Validation of a Model for the Mechanics of Paper". Technical University Eindhoven, 2023.

[14] Sören Östlund and Kaarlo Niskanen. *Mechanics of Paper Products*. Berlin, Boston: De Gruyter, 2021. DOI: doi:10.1515/9783110619386.

[15] P.E.J. Ploumen. "A three dimensional pore network model to predict the permeability of paper". Technical University Eindhoven, 2022.

[16] Lisa A Richards. "Capillary conduction of liquids through porous mediums". In: *Journal of Applied Physics* 1 (1931), pp. 318–333. ISSN: 0148-6349. DOI: 10.1063/1.1745010.

[17] Joachim Schoelkopf and G. Peter Matthews. "Influence of inertia on liquid absorption into paper coating structures". In: *Nordic Pulp & Paper Research Journal* 15.5 (2000), pp. 422–430. DOI: doi:10.3183/npprj-2000-15-05-p422-430.

[18] C. G. van der Sman. "Modeling moisture-induced deformation of printing paper sheets". Technical University Eindhoven, 2014.

[19] Lijun Su et al. "Approximate solution of a one-dimensional soil water infiltration equation based on the Brooks-Corey model". In: *Geoderma* 297 (2017), pp. 28–37. ISSN: 0016-7061. DOI: 10.1016/j.geoderma.2017.02.026.

[20] M.R. van der Wijst. "Deriving effective macro-scale transport properties of water penetration through a paper sheet". Technical University Eindhoven, 2022.

[21] X. Yin et al. “Droplet Imbibition into Paper Coating Layer: Pore-Network Modeling Simulation”. In: *Transport in Porous Media* 125.2 (2018), pp. 239–258. DOI: 10.1007/s11242-018-1116-0.

A Derivation Richards equation

Richards equation is derived from the general mass balance equation. According to this equation, the mass accumulation over time is a function of the incoming and outgoing mass fluxes. In terms of mol it is expressed as,

$$\frac{\partial}{\partial t}\int_V n dV = -\oint_S \vec{J}\cdot\vec{n} dS. \tag{A.1}$$

Where the first term represents the mass accumulation, and the second term the in and outgoing mass flux. The variable n represents the amount of mol per volume $[\frac{mol}{m^3}]$, $\vec{J}$ the flux $[\frac{mol}{m^2 s}]$ and $\vec{n}$ the normal vector. Note that the in going flow is negative and the outgoing flow positive, as is shown in Figure A.1.

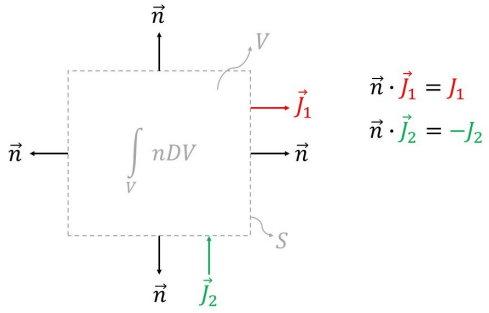

Figure A.1: Schematic of mass balance.

The divergence theorem can be used to express Equation A.1 in terms of two volume integrals,

$$\frac{\partial}{\partial t}\int_V n dV = -\int_V \nabla\cdot\vec{J} dV. \tag{A.2}$$

From this follows that,

$$\frac{\partial n}{\partial t} = -\nabla\cdot\vec{J}. \tag{A.3}$$

The local fluid content in the pores and the volumetric inflow can be written in terms of n and $\vec{J}$ through multiplication of the molarity v,

$$\chi_p = vn \tag{A.4a}$$

$$\vec{q} = v\vec{J}. \tag{A.4b}$$

Combining Equation A.3 and Equation A.4 leads to,

$$\begin{aligned}\frac{\partial \chi_p}{\partial t} &= -\nabla\cdot\vec{q}\\ \phi_p\frac{\partial S_p}{\partial t} &= -\nabla\cdot\vec{q}.\end{aligned} \tag{A.5}$$

Applying Darcy's equation and writing in one-dimension leads to,

$$\phi_p\frac{\partial S_p}{\partial t} = \frac{\partial}{\partial z}\Big(\frac{K_p(S_p)}{\eta}\frac{\partial p_c(S_p)}{\partial z}\Big). \tag{A.6}$$

Taking into consideration that the total pressure can be expressed in terms of the capillary pressure,

$$p(z,t) = p_{amb} - p_c(z,t). \tag{A.7}$$

Equation A.6 can be written in terms of the capillary pressure, which leads to the Richards equation,

$$\phi_p\frac{\partial S_p}{\partial t} = -\frac{\partial}{\partial z}\Big(\frac{K_p(S_p)}{\eta}\frac{\partial p_c(S_p)}{\partial z}\Big). \tag{A.8}$$

B Derivation pore size distribution

Assuming that the porous network is made from a bundle of parallel tubes, the intruded volume can be written as the summation of each tube's volume,

$$V_{pl}(r) = L_p \int_0^r P(r)\pi r^2 dr \tag{B.1}$$

here it is important to include the pore size distribution, which is a measure for how much tubes with radius r are present in the porous medium. Taking the derivative of the volume with respect to r leads to the following,

$$\begin{aligned} \frac{dV_{pl}}{dr} &= L_p P(r)\pi r^2 \\ P(r) &= \frac{1}{L_p \pi r^2}\frac{dV_{pl}}{dr}. \end{aligned} \tag{B.2}$$

The intruded volume can also be expressed in terms of the saturation, by multiplying it with the total pore volume,

$$V_{pl}(r) = V_p S_p(r). \tag{B.3}$$

The pore size distribution can thus also be expressed in terms of the saturation, by taking the derivative with respect to r in Equation B.3 and substituting the result in Equation B.2,

$$P(r) = \frac{V_p}{L_p \pi r^2}\frac{dS_p}{dr}. \tag{B.4}$$

C Determining water retention parameters

Parameters for the three water retention functions are determined from the experimental MIP results. Here an example is shown on how to derive these parameters. For this example, experimental results are taken from a MIP test performed on a Mondi CF paper type.
As a first step, the resulting water retention curve from the MIP test is mirrored around 0.5 saturation. In the MIP test the largest pores are filled first, due to these having the least pressure gradient. When applying an external pressure the mercury thus first invades these pores. When applying a liquid with a low contact angle, such as demiwater, no external pressure is needed as the liquid gets sucked into the porous medium. This process happens in the pores with the largest pressure gradient, as they suck in the liquid the hardest. In this case the smallest pores are thus filled at first. Due to this opposition it is needed to mirror the curve from the MIP test. The derived curve is shown with the results from the MIP experiments in Figure C.1

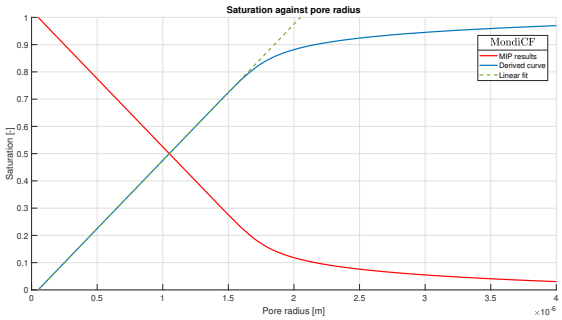

Figure C.1: Water retention function from MIP result.

C.1 Linear model

The linear model is fitted on the linear part of the derived curve. The linear fit is written in the form,

$$S_{p,Linear}(r) = \frac{r - r_{min}}{r_{max} - r_{min}}. \tag{C.1}$$

The value for r_{min} is thus equal to the measured radius at which the saturation is zero. The value for r_{max} can then be determined from the slope of the linear part of measured water retention curve,

$$r_{max} = \left(\frac{dS_p}{dr}\right)^{-1} + r_{min}. \tag{C.2}$$

The linear fit is visually depicted in Figure C.1

C.2 Brooks-Corey model

The Brooks-Corey model, describes the relation between capillary pressure and saturation for values of the capillary pressure higher than the bubbling pressure. The bubbling pressure is the pressure that needs to be applied on the gas phase to remove an initial amount of water in a fully saturated porous medium. In the work of Su [19], for capillary pressure lower than the bubbling pressure the saturation is set equal to one, which leads to the following equation for the Brooks-Corey model,

$$S_{p,BC}(p_c) = \begin{cases} 1 & p_c < p_b \\ \left(\frac{p_b}{p_c}\right)^{\lambda} & p_c \geq p_b. \end{cases} \tag{C.3}$$

Within this relation the parameters p_b and λ need to be determined. The two parameters are medium dependent and are a measure for the maximum pore size forming and characterization of

the pore size distribution respectively. In order to fit these parameters to measurement data the following procedure is followed. First the following derivative on loglog-scale is determined,

$$\frac{dlog_{10}(S_p)}{dlog_{10}(p_c)} = (ln10)p_c\frac{dlog_{10}(S_p)}{dp_c}. \tag{C.4}$$

The last term in Equation C.4 is given by,

$$\begin{aligned}\frac{dlog_{10}(S_p)}{dp_c} &= \frac{d}{dp_c}\Big(\frac{ln\Big(\big(\frac{p_b}{p_c}\big)^{\lambda}\Big)}{(ln10)}\Big) \\ &= -\frac{1}{(ln10)}\Big(\frac{p_b}{p_c}\Big)^{-\lambda}\lambda\Big(\frac{p_b}{p_c}\Big)^{(\lambda-1)}\frac{p_b}{p_c^2} \\ &= -\frac{\lambda}{(ln10)p_c}.\end{aligned} \tag{C.5}$$

Substituting Equation C.5 into Equation C.4 then gives,

$$\frac{dlog_{10}(S_p)}{dlog_{10}(p_c)} = -\lambda. \tag{C.6}$$

Plotting the Brooks-Corey water retention function on a loglog-scale thus results in a straight line with slope $-\lambda$. The Brooks-Corey function is thus linearly fitted on the measured water retention curve displayed on a loglog-scale. This is visually depicted in Figure C.2.

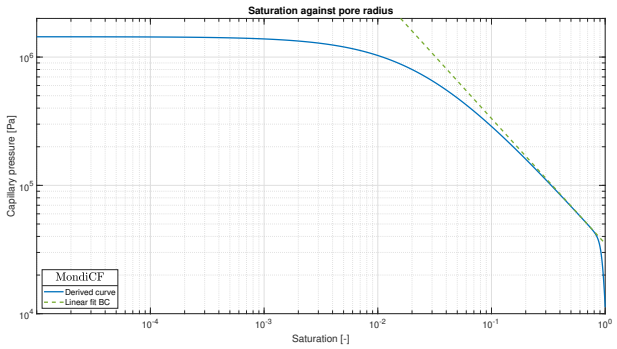

Figure C.2: Water retention function Brooks-Corey fit.

C.3 van Genuchten model

Unlike the two models mentioned above, the van Genuchten model is valid for all values of p_c. Instead of a discontinuous jump at the bubbling pressure, smoothing is added in this model, which leads to a continuous curve that approximately goes to one for low capillary pressures. The van Genuchten model is given by,

$$S_{p,VG} = \big(\frac{1}{1+(\alpha p_c)^n}\big)^m. \tag{C.7}$$

The relation consist of three unknown parameters, α, m and n. For the special case that the van Genuchten model can be used in the Mualem theory [12], a relation exists between the parameters m and n,

$$n = \frac{1}{1-m}. \tag{C.8}$$

Using Equation C.8, the van Genuchten relation can be rewritten to find an expression for α in terms of saturation, capillary pressure and the unknown parameter m,

$$\alpha = \frac{1}{p_c}(S_p^{-\frac{1}{m}} - 1)^{\frac{1}{n}}. \tag{C.9}$$

The parameters α and n can thus be determined if m is known. To determine parameter m from the measurements, the following procedure is used.
First, Equation C.7 is rewritten as,

$$\frac{\chi - \chi_r}{\chi_s - \chi_r} = \big(\frac{1}{1 + (\alpha p_c)^n}\big)^m \tag{C.10}$$

where χ is the water content. The subscripts s and r refer to the saturated and residual water content of the porous medium. The saturated water content refers to the water content if the porous medium is fully saturated. This value equals the porosity of the medium. The residual water content is the initial water content in the porous medium.
From Equation C.10, the water content can be written as a function of the capillary pressure,

$$\chi = \chi_r + \frac{\chi_s - \chi_r}{[1 + (\alpha p_c)^n]^m}. \tag{C.11}$$

Differentiation gives,

$$\begin{aligned} \frac{d\chi}{dp_c} &= -\alpha m n(\chi_s - \chi_r)\frac{(\alpha p_c)^{n-1}}{[1 + (\alpha p_c)^n]^m} \\ &= -\frac{\alpha m(\chi_s - \chi_r)}{1 - m} S_p^{\frac{1}{m}}(1 - S_p^{\frac{1}{m}})^m. \end{aligned} \tag{C.12}$$

Substitution of Equation C.9 into Equation C.12 leads to,

$$p_c\frac{d\chi}{dp_c} = -\frac{m(\chi_s - \chi_r)}{1 - m} S_p(1 - S_p^{\frac{1}{m}}). \tag{C.13}$$

The first term in Equation C.13 is related to the slope on the semi-logp_c graph of the retention curve,

$$\frac{d\chi}{d(log_{10}(p_c))} = (ln10)p_c\frac{d\chi}{dp_c}. \tag{C.14}$$

The derivative of the saturation with respect to the logarithm of capillary pressure can also be evaluated and is related to the slope of the semi-logp_c graph of the retention curve,

$$\begin{aligned} \frac{dS_p}{d(log_{10}(p_c))} &= \frac{1}{\chi_s - \chi_r}\frac{d\chi}{d(log_{10}(p_c))} \\ &= -(ln10)\frac{m}{1 - m} S_p(1 - S_p^{\frac{1}{m}}). \end{aligned} \tag{C.15}$$

The parameters α and m can now be determined by taking a point A on the water retention curve. At point A the values for saturation, capillary pressure and the derivative of saturation with respect to capillary pressure needs to be evaluated. The best location for evaluating these values is halfway between χ_r and χ_s, so at $S_p = 0.5$. This is visually depicted in Figure C.3. By doing this the parameters α and m can be determined with the following two equations,

$$\frac{dS_p}{d(log_{10}(p_c))} = -\frac{1}{2}(ln10)\frac{m}{1 - m}(1 - 2^{-\frac{1}{m}}) \tag{C.16}$$

$$p_c = \frac{1}{\alpha}(2^{\frac{1}{m}} - 1)^{1-m}. \tag{C.17}$$

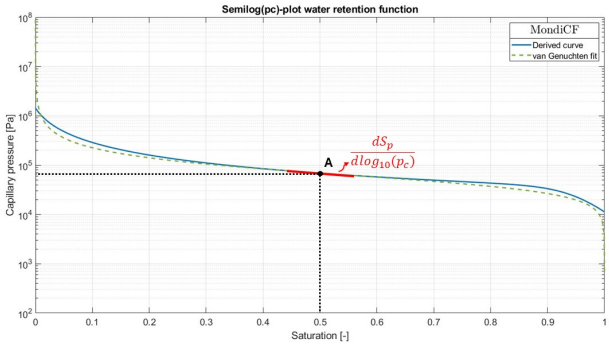

Figure C.3: Water retention function van Genuchten fit.

To determine parameter m from Equation C.16 it is convenient to express m as of function of the slope $T = \frac{dS_p}{d(logp_c)}$. In the work of van Genuchten two empirical inversion formulas are proposed,

$$m = \begin{cases} 1 - exp(-0.8T), & (0 < T \leq 1) \\ 1 - \frac{0.5755}{T} + \frac{1}{T^2} + \frac{0.025}{T^3}, & (T > 1). \end{cases} \tag{C.18}$$

By approximating the slope on the semilogp_c water retention curve the parameter m can thus be determined. The values α and n can thereafter be derived from Equation C.9 and Equation C.8 respectively.

D Permeability models

Darcy's equation is used to describe flow trough a porous medium. Within darcy's equation a variable called the permeability is used, which describes the resistance against flow in the porous medium. It is in important measure in determining the flux through a porous block. Darcy's equation, in one dimension, is given by,

$$q_p = -\frac{K_p}{\eta}\frac{dp}{dz}. \tag{D.1}$$

The derivation of permeability is presented here for two models proposed by N. Dave et al. [4] and van Genuchten [8]. Dave's model is based on the linear part of the experiment results obtained from a MIP test. This model is also referred to as the linear model. Van Genuchten's model is built upon equations derived from Mualem's model [12], which is formulated based on knowledge of the water retention curve and the conductivity at saturation.

D.1 Linear model

The linear model assumes that the porous medium is made of a bundle of parallel tubes with different radii, the total flux can be expressed as the summation of volume flux's in each cylinder Q_i divided by the total area A,

$$q_p = -\frac{\sum_{i=1}^{N_{pl}} Q_i}{A} = -\sum_{i=1}^{N_{pl}} \frac{\pi r_i^4}{8\eta A}\frac{dp}{dz}. \tag{D.2}$$

It is important to note here that the summation is taking over all cylinders that are filled with liquid, N_{pl}. In the cylinders where no water is available, no flux is present.
The porosity of the porous medium is defined as,

$$\phi_p = \frac{V_p}{V} = \frac{\sum_{i=1}^{N_p} \pi r_i^2}{A} \tag{D.3}$$

here the summation is taken over all pores N_p, as the porosity is dependent on all pores inside the porous medium. Rewriting Equation D.3 in terms of A and substituting the result in Equation D.2 gives,

$$q_p = -\frac{\phi_p}{8\eta}\frac{\sum_{i=1}^{N_{pl}} r_i^4}{\sum_{i=1}^{N_p} r_i^2}\frac{dp}{dz}. \tag{D.4}$$

From comparing Equation D.4 with Equation D.4 it becomes clear that the permeability for a bundle of parallel tubes with different radii is given by,

$$\begin{aligned} K_p &= \frac{1}{8}\phi_p \frac{\sum_{i=1}^{N_{pl}} r_i^4}{\sum_{i=1}^{N_p} r_i^2} \\ &= \frac{1}{8}\phi_p \frac{\int_0^r P(\rho)\rho^4 d\rho}{\int_0^\infty P(r) r^2 dr} \\ &= \frac{\frac{V_p}{L_p \pi}\int_0^r \frac{dS_p}{d\rho}\rho^2 d\rho}{\frac{V_p}{L_p \pi}\int_0^\infty \frac{dS_p}{dr} dr} \\ &= \frac{\int_0^r \frac{dS_p}{d\rho}\rho^2 d\rho}{\int_0^\infty \frac{dS_p}{dr} dr}. \end{aligned} \tag{D.5}$$

Taking the derivative of the saturation S_p with respect to the pore size r for the linear model gives,

$$\frac{dS_p}{dr} = \frac{1}{r_{max} - r_{min}}. \tag{D.6}$$

So the resulting permeability is,

$$K_p = \frac{1}{24}\phi_p \frac{r^3 - r_{min}^3}{r_{max} - r_{min}}. \tag{D.7}$$

Writing r_{wet} in terms of S_p and multiplying the permeability by a correction factor $\frac{1}{c_{perm}}$ leads to the final function for the permeability,

$$K_p(S_p) = \frac{\phi_p}{24 c_{perm}} \frac{\big(r_{min} + S_p(r_{max} - r_{min})\big)^3 - r_{min}^3}{r_{max} - r_{min}}. \tag{D.8}$$

D.2 van Genuchten model

The van Genuchten model gives a measure for the relative permeability as a function of capillary pressure based on the theory outlined in Mualem's model. Relative permeability represents the ratio of effective permeability to saturated permeability and ranges between zero and one. A value of one indicates that the effective permeability equals the saturated permeability, i.e. the permeability of a fully saturated porous medium. The expression for relative permeability is as follows:

$$K_r = \frac{K_p}{K_{sat}} \tag{D.9}$$

with K_{sat} the saturated permeability. The equation derived by Mualem [12] for predicting the this hydraulic conductivity is,

$$K_r = S_p^{\frac{1}{2}} \Big[\frac{\int_0^{S_p} \frac{1}{p_c(z)} dz}{\int_0^1 \frac{1}{p_c(z)} dz} \Big]^2. \tag{D.10}$$

Van Genuchten integrated this expression with his relation for the water retention curve. From this he derived an expression for the relative permeability in terms of capillary pressure,

$$K_r(p_c) = \frac{\{1 - (\alpha p_c)^{n-1}[1 + (\alpha p_c)^n]^{-m}\}^2}{[1 + (\alpha p_c)^n]^{\frac{m}{2}}}. \tag{D.11}$$

Expressing capillary pressure in terms of saturation gives a relation for relative permeability in terms of saturation. Subsequently, the effective permeability K_p is obtained by multiplying this relative permeability by the saturated permeability. The saturated permeability is determined from the total permeability of the linear model, which involves substituting a value of one into Equation D.8. Thus, the saturated permeability is expressed as:

$$K_{sat} = \frac{\phi_p}{24 c_{perm}} \frac{r_{max}^3 - r_{min}^3}{r_{max} - r_{min}}. \tag{D.12}$$

E Global fiber saturation

To transform from the local fiber saturation to a global fiber saturation of the paper sheet the cross section at a height z is considered. When a specific pore is saturated it starts to fill its neighbouring fiber. It is assumed that a single pore fills this neighbouring fiber till a depth d, which equals half the fiber thickness. The volume that a single pore can fill according to this assumption is visually depicted in Figure E.1 by the red dashed line. The total fiber volume can then be estimated by adding all local fiber volumes,

$$V_f = \sum_{i=1}^{N} d\Delta A_i \tag{E.1}$$

where ΔA is the local area between a specific pore and its neighbouring fiber.

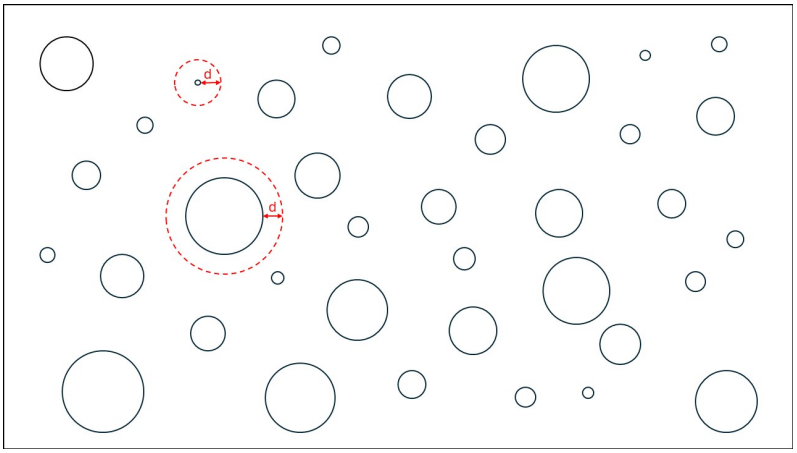

Figure E.1: Schematic cross section paper sheet with simplified pore structure.

Adding the total fiber volume to the total pore volume gives the volume of the paper sheet. From this expression it is possible to write the total fiber volume as a function of the pore size distribution $P(r)$,

$$\begin{aligned} V_f &= V - V_p \\ &= (\frac{1}{\phi_p} - 1)V_p \\ &= (\frac{1}{\phi_p} - 1)L_p \int_0^\infty P(r)\pi r^2 dr. \end{aligned} \tag{E.2}$$

When assuming that the pores are cylindrical shaped, the local area ΔA between pore and fiber can be estimated as a fraction of the outer surface of a cylinder. This surface is given by the circumference of the cylinder times the characteristic length L_p,

$$\Delta A = c_A 2\pi r L_p \tag{E.3}$$

where c_A describes the fraction of the area. This fraction can be found by combining Equation E.1, Equation E.2 and Equation E.3,

$$\begin{aligned} \sum_{i=1}^{N} c_A 2\pi r_i L_p d &= (\frac{1}{\phi_p} - 1)L_p \int_0^\infty P(r)\pi r^2 dr \\ c_A L_p d \int_0^\infty P(r) 2\pi r dr &= (\frac{1}{\phi_p} - 1)L_p \int_0^\infty P(r)\pi r^2 dr \\ c_A &= \frac{1-\phi_p}{\phi_p d} \frac{\int_0^\infty P(r)\pi r^2 dr}{\int_0^\infty P(r) 2\pi r dr}. \end{aligned} \tag{E.4}$$

From this the ratio of wetted surface area can be determined as,

$$\begin{aligned}\frac{\sum_{i=1}^{N_w}\Delta A_i}{V_f} &= \frac{\sum_{i=1}^{N_w} c_A 2\pi r_i L_p}{(\frac{1}{\phi_p}-1)L_p\int_0^\infty P(r)\pi r^2 dr}\\ &= c_A\frac{\phi_p}{1-\phi_p}\frac{\int_0^r P(\rho)2\pi\rho d\rho}{\int_0^\infty P(r)\pi r^2 dr}\\ &= \frac{\int_0^r P(\rho)2\pi\rho d\rho}{d\int_0^\infty P(r)2\pi r dr}\\ &= \frac{\ln\Big(1+S_p\frac{r_{max}-r_{min}}{r_{min}}\Big)}{\ln\Big(\frac{r_{max}}{r_{min}}\Big)d}.\end{aligned} \tag{E.5}$$